Icarus 211 (2011) 655–671

Contents lists available at ScienceDirect

Icarus

journal homepage: www.elsevier.com/locate/icarus

Transient surface liquid in Titan's polar regions from Cassini

A.G. Hayes [a,*], O. Aharonson [a], J.I. Lunine [b], R.L. Kirk [c], H.A. Zebker [e], L.C. Wye [e], R.D. Lorenz [d], E.P. Turtle [d], P. Paillou [f], G. Mitri [a], S.D. Wall [g], E.R. Stofan [h], K.L. Mitchell [g], C. Elachi [g], the Cassini RADAR Team

[a] Division of Geological and Planetary Sciences, California Institute of Technology, 1200 E. California Blvd., Pasadena, CA 91125, United States
[b] Dipartimento di Fisica, Università degli Studi di Roma "Tor Vergata", Via della Ricerca Scientifica 1, 00133 Roma, Italy
[c] Astrogeology Team, United Stated Geological Survey, 2255 N. Gemini Dr., Flagstaff, AZ 86001, United States
[d] Applied Physics Laboratory, John Hopkins University, 11100 Johns Hopkins Road, Laurel, MD 20723, United States
[e] Electrical Engineering, Stanford University, 350 Serra Mall, Stanford, CA 94305, United States
[f] Laboratoire d'Astrophysique de Bordeaux, Université de Bordeaux, UMR5084, Floirac, France
[g] Jet Propulsion Laboratory, California Institute of Technology, 4800 Oak Grove Dr., Pasadena, CA 91109, United States
[h] Proxemy Research, 20528 Farcroft Lane, Gaithersburg, MD 20882, United States

ARTICLE INFO

Article history:
Received 7 December 2009
Revised 16 August 2010
Accepted 22 August 2010
Available online 25 September 2010

Keywords:
Titan
Saturn, Satellites
Radar observations
Infrared observations

ABSTRACT

Cassini RADAR images of Titan's south polar region acquired during southern summer contain lake features which disappear between observations. These features show a tenfold increases in backscatter cross-section between images acquired one year apart, which is inconsistent with common scattering models without invoking temporal variability. The morphologic boundaries are transient, further supporting changes in lake level. These observations are consistent with the exposure of diffusely scattering lakebeds that were previously hidden by an attenuating liquid medium. We use a two-layer model to explain backscatter variations and estimate a drop in liquid depth of approximately 1-m-per-year. On larger scales, we observe shoreline recession between ISS and RADAR images of Ontario Lacus, the largest lake in Titan's south polar region. The recession, occurring between June 2005 and July 2009, is inversely proportional to slopes estimated from altimetric profiles and the exponential decay of near-shore backscatter, consistent with a uniform reduction of 4 ± 1.3 m in lake depth.

Of the potential explanations for observed surface changes, we favor evaporation and infiltration. The disappearance of dark features and the recession of Ontario's shoreline represents volatile transport in an active methane-based hydrologic cycle. Observed loss rates are compared and shown to be consistent with available global circulation models. To date, no unambiguous changes in lake level have been observed between repeat images in the north polar region, although further investigation is warranted. These observations constrain volatile flux rates in Titan's hydrologic system and demonstrate that the surface plays an active role in its evolution. Constraining these seasonal changes represents the first step toward our understanding of longer climate cycles that may determine liquid distribution on Titan over orbital time periods.

1. Introduction

Titan's active methane-based hydrologic cycle is unique among the extraterrestrial bodies of our Solar System. As such, observing seasonal variations in Titan's volatile system is the primary goal of the Cassini spacecraft's Equinox (2008–2010) and Solstice (2010–2017) missions (Brown et al., 2010). Herein we describe the discovery of ephemeral liquid disappearing from the surface of Titan during southern summer. Our observations include a collection of transient lacustrine features as well as a recession in the shorelines of Ontario Lacus. Observations were acquired using the Ku-Band Cassini RADAR (λ = 2.2 cm) and returns are used to model liquid depths and link surface change to theoretical predictions of volatile transport in Titan's hydrologic system. These ephemeral features represent direct evidence for surface liquid playing an active role in Titan's methane cycle.

Lacustrine features identified on Titan (Stofan et al., 2007; Hayes et al., 2008; Mitchell et al., in preparation) have been grouped into three classes: empty lake basins, partially filled lakes, and dark or liquid-filled lakes (Hayes et al., 2008). Partially filled lakes have radar returns consistent with incident radiation penetrating a liquid layer and interacting with the lakebed, while dark lakes completely reflect and absorb the incident microwave energy (Hayes et al., 2008; Paillou et al., 2008b). Empty lakes are brighter than their exteriors in both nadir and off-nadir observations, suggesting compositional variations. Higher relative backscatter

* Corresponding author. Fax: +1 626 568 0935.
E-mail address: hayes@gps.caltech.edu (A.G. Hayes).

0019-1035/$ - see front matter © 2010 Elsevier Inc. All rights reserved.
doi:10.1016/j.icarus.2010.08.017

at large off-nadir angles ($\theta > 30°$) also suggests a stronger volume scattering component (Hayes et al., 2008). All lakes are restricted to latitudes poleward of 55° and cover 1.5% of Titan's observed surface. There is a significant dichotomy in polar lake distributions, with dark lakes covering 10% of the area in the north but only 0.4% in the south (poleward of 55°) (Hayes et al., 2008; Aharonson et al., 2009). Aharonson et al. (2009) attributes this dichotomy to an a seasonal asymmetry in incident flux caused by Saturn's eccentricity and Titan's solar longitude of perihelion. Observed ephemeral features are initially consistent with partially filled lakes and later transition into features similar to empty lake basins.

Ephemeral features are located in the south polar region (55–90°S), where 9% of the surface has been observed by multiple Synthetic Aperture Radar (SAR) swaths. Including ~1 km/pixel high altitude SAR (HiSAR) measurements (West et al., 2008), the repeat coverage increases to 32%. Between October 2004 (Cassini flyby TA) and January 2010 (T65), the Cassini spacecraft has acquired SAR images, at a resolution of ~300 m/pixel, covering 35% of Titan's surface and 45% of the areas poleward of 55°. Including HiSAR, the global and polar coverage increases to 45% and 60%, respectively. These radar observations allow for the identification and analysis of temporal variation in the polar regions with baselines of up to 3 years. We identify and model examples of transient surface liquid observed by the RADAR instrument and compare estimated loss rates to global circulation models (GCM). During the observation period (September 2005–January 2010), Titan's south polar region was in summer and expected to be in a state of volatile evaporation (Mitchell, 2008; Newman et al., 2008). Available repeat coverage of the north polar region allows us to identify only one area where surface change can be unambiguously separated from variations in observational geometry, although additional observations of the north are planned during Cassini's Solstice Mission.

Below, we present observations, analyses, and their implications. Section 2 describes the analysis and modeling of the backscatter from lacustrine features in preparation for comparison against observed ephemeral features. Section 3 describes the details of the ephemeral feature observations and their viewing geometries, including morphologic descriptions and the implications of Ontario Lacus shoreline recession. In Section 3 we also develop a simple two-layer model in order to estimate the changes in lake levels required by the radar data. Potential explanations for the surface change, their implications regarding Titan's volatile system, and comparison to previous theoretical predictions are described in Section 4.

2. Radar backscatter of lacustrine features on Titan

The disappearance or alteration of lacustrine features may result from two classes of explanations. The first is observational or instrumental effects; the second is physical changes on the surface of Titan. Observational effects include variation in radar backscatter due to different incidence, azimuth, and polarization angles between Titan passes. Backscatter can vary significantly as a function of these angles, depending on surface and subsurface properties such as composition, roughness, and degree of volume scattering. The possibility that these effects are the only important phenomena determining backscatter variation will be referred to as the null hypothesis. Alternatively, ephemeral observations may be due to surface changes including liquid evaporation, infiltration, freezing, wave activity, and cryovolcanism.

In order to discount the null hypothesis as an explanation for observed changes, we will review the backscatter variations from all lacustrine features on Titan and use their response as a comparison point for discussing ephemeral feature backscatter in Section 3. The microwave reflectivity of Titan's surface is reported using the normalized backscatter cross-section (σ_o), a non-dimensional quantity that describes received radar power as compared to an isotropically scattering surface. In order to derive σ_o, an effective area is defined that is equal to the size of the isotropic scatterer required to produce the measured power. The effective area is then divided by the imaged surface area to create a non-dimensional σ_o (Ulaby et al., 1982).

The normalized backscatter cross-section of the icy Galilean satellites show that they are diffusely scattering bodies dominated by complex volume scattering within a porous icy regolith (Black et al., 2001; Ostro et al., 1992). When viewed at resolutions comparable to their radius, the saturnian satellites Enceladus, Tethys, Dione, Rhea, Iapetus, Hyperion, and Phoebe are also dominated by diffuse scattering and have comparable electrical properties to their Galilean counterparts (Ostro et al., 2006). Terrains on Titan, however, have a surface term which requires a Kirchhoff scattering component in addition to the expected diffuse behavior (Campbell et al., 2003; Wye et al., 2007; Janssen et al., 2009). Sufficiently accurate high-resolution data do not exist to see if this is also true for the other saturnian satellites. Kirchhoff scattering is common among the inner Solar System bodies (Muhleman, 1995) and attributed to quasi-specular Fresnel reflection off surface facets which are oriented toward incoming radiation and smooth compared to the radar wavelength (Beckmann and Spizzichino, 1963; Wye et al., 2007).

Quasi-specular backscatter is typically modeled by a surface whose elevation departure from a smooth, perfectly conducting plane follows a Gaussian probability distribution (Elachi and van Zyl, 2006). The horizontal structure of this surface is often described using an autocorrelation function. One commonly used autocorrelation function is also Gaussian (Hargreaves, 1959) and produces a backscatter model of the form (denoted Gaussian):

$$\sigma_{o,\ \mathrm{Gauss}} = \frac{\rho C}{\cos^4\theta} e^{-C\tan^2\theta} \tag{1}$$

where ρ is the Fresnel reflection coefficient at normal incidence, $C^{-1/2}$ is the surface RMS slope, and θ is the incidence angle. The constant C is described using a tilt angle θ_{RMS} such that $C^{-1} = \tan^2\theta_{\mathrm{RMS}}$. Another common autocorrelation function is exponential (Daniels, 1961) and yields the Hagfors scattering model (Hagfors, 1964):

$$\sigma_{o,\ \mathrm{Hag.}} = \frac{\rho C}{2\cos^6\theta}\left[1 + C\left(\frac{\tan\theta}{\cos\theta}\right)^2\right]^{-3/2} \tag{2}$$

The Hagfors model is commonly used to describe radar backscatter from the lunar surface (Hagfors, 1970; Simpson and Tyler, 1982) while the Gaussian model has been shown to fit radar returns from portions of the venusian surface (Tyler et al., 1992; Sultan-Salem and Tyler, 2006). The Hagfors model has also been used to model the specular portions of radar returns from Titan (Campbell et al., 2003; Wye et al., 2007). Other quasi-specular backscatter models can be derived by assuming other forms for the autocorrelation function.

Diffuse backscatter generally dominates radar echoes at large incidence angles ($\theta > 30°$) while facet scattering dominates at low incidence angles (Elachi and van Zyl, 2006). Diffuse backscatter can arise from small-scale surface roughness and/or subsurface volume scattering and is typically modeled using a cosine to-a-power of the form:

$$\sigma_{o,\ \mathrm{Diff.}} = A\cos^n\theta \tag{3}$$

where A is a the diffuse signal power and n is the cosine power. Fits to early Cassini scatterometry observations of Titan at large incidence angles yield $A = 0.34$ and $n = 1.22$ for the combined dataset (Wye et al., 2007). These values are consistent with previously

published values for the icy Galilean and saturnian satellites (Wye et al., 2007). Polarization and azimuth angle effects are neglected in both the quasi-specular and diffuse models presented above.

We use two-component models consisting of quasi-specular (Hagfors or Gaussian) and diffuse components to describe radar backscatter values for both empty and partially filled lake features on Titan. Fig. 1 shows the backscatter values for 110 empty lakes and 101 partially filled lakes distributed throughout the polar regions. Both distributions can be described using the sum of a Gaussian quasi-specular and a diffuse component. Because SAR data are rarely acquired much above 40° incidence, we cannot properly estimate the diffuse component from these data alone. For this reason, we presume a cosine power law of $n = 1.22$, equivalent to that estimated by Wye et al. (2007), and allow the amplitude of the diffuse term to vary. Hagfors models do not match the lake data as well as the Gaussian model at low incidence angles. Average backscatter values for the regions immediately surrounding the lake features are best fit using a Hagfors quasi-specular component. The model parameters for the surrounding regions are found to be similar to those derived by Wye et al. (2007) using Cassini scatterometry for regions elsewhere on Titan's surface. We plot the best-fit models for lake features as dashed lines in Fig. 1 and list model parameters in Table 1.

The empty lake observations are self-consistent within their feature class and distinct from the partially filled lake radar returns. The amplitude of the diffuse scattering term for the empty lake data ($A_{\text{emp Gauss}} = 0.55 \pm 0.07$, $A_{\text{emp Hag.}} = 0.41 \pm 0.12$) was significantly higher than the best fit for the surrounding region ($A_{\text{sur Gauss}} = 0.38 \pm 0.03$, $A_{\text{sur Hag.}} = 0.34 \pm 0.04$) and partially filled lakes ($A_{\text{par Gauss}} = 0.11 \pm 0.02$, $A_{\text{par Hag.}} = 0.06 \pm 0.04$). It is important to note, however, that a non-zero diffuse scattering component is required to accurately describe all observed features. The increase in diffuse scattering for the empty lakebeds, as compared to the surrounding terrain, can be used as a constraint for formation hypothesis. One hypothesis, discussed in Mitchell et al. (in preparation), suggests that these features are formed through karstic dissolution. Dissolution chemistry would produce higher porosity and subsurface structure beneath lakebeds, enhancing their diffuse volume scattering. However other hypotheses, such as cracking in evaporative lakebed deposits, may also be consistent with the observed backscatter variations. Fig. 2 shows backscatter values for an empty lake and a partially filled lake which were observed at multiple incidence angles. Both features were observed in the north polar region during the winter season when Mitchell (2008), Newman et al. (2008), and Graves et al. (in preparation) predict evaporation and precipitation to be minimal. The predictions of Tokano (2009b) vary based on predominate liquid composition. In the case of ethane-rich seas (<17%CH_4), Tokano (2009b) also predicts winter evaporation over the northern lakes to be minimal. For methane-rich seas (>62%CH_4), however, Tokano (2009b) predicts evaporation to be at its peak during the winter season. Observations of the north polar region acquired in December 2009 (T64) show no unambiguous examples of surface change, supporting Mitchell (2008), Newman et al. (2008), and Graves et al. (in preparation) (Section 3). Observations of the empty lake depicted in Fig. 2 were acquired over a period of 9 months and the best-fit model parameters (holding the cosine power constant) have values similar to the empty lake class (Table 1). The partially filled lake, which was observed over a period of 7 months, shows no change in its morphologic boundaries and has backscatter variation consistent with a Gaussian plus diffuse scattering model with parameters similar to that of the partially filled lake class.

The shape of the quasi-specular scattering component is determined by the roughness parameter C. For large values of C (small θ_{RMS}) the point at which the backscatter function transitions from steep to shallow dependence on incidence moves towards lower angles. For a given incidence angle, there is a maximum value of C beyond which the backscatter decreases, requiring an increase in the Fresnel reflection coefficient, and hence dielectric constant, in order to account for the increase in σ_o. To adequately match the radar returns of empty lake basins and surrounding terrain at low incidence angles, dielectric constants of ~3 are required. Passive radiometry observations suggest real dielectric constants $\epsilon_r = 1.7 \pm 0.2$ for most of the equatorial and polar regions of Titan (Elachi et al., 2005; Janssen et al., 2009). The Permittivity, Waves, and Altimetry (PWA) instrument onboard the Huygens probe also found a surface dielectric constant of ~2 (Grard et al., 2006). While the PWA operates at kilohertz as opposed to gigahertz frequencies, the real dielectric constant of most Titan-relevant materials, including water ice and hydrocarbon, is relatively consistent over this range at 95 K (Grard et al., 2006; Sen et al., 1992). The composition of terrain in Titan's polar regions is expected to be a porous mixture of water ice ($\epsilon_r = 3.13$), tholin ($\epsilon_r = 2.0$–2.4), and liquid hydrocarbon ($\epsilon_r = 1.7$–1.9) (Lunine, 1993; Paillou et al., 2008a; Thompson and Squyres, 1990). While model parameters derived here are consistent with the upper end of dielectric constants for these materials, they should not be taken at face value given that we lack very low-angle data ($\theta < 10°$) and proper estimates of the diffuse component. Composite dielectric constants greater than 3 are not expected and the quasi-specular scattering models

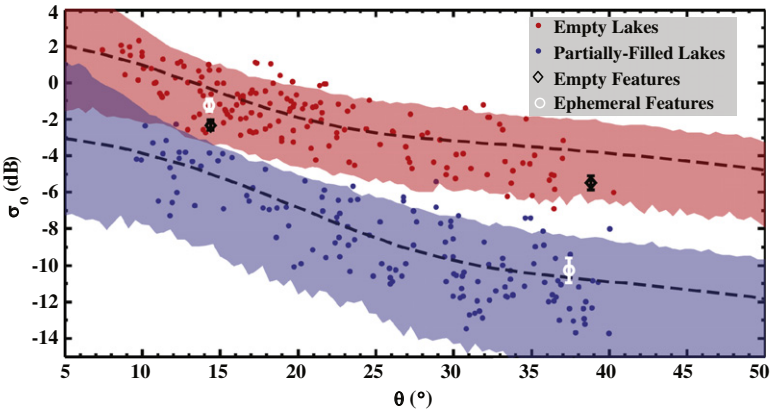

Fig. 1. σ_o values for partially filled and empty lakes observed on Titan. Red and blue shading represent 95% confidence interval in model output of the mean backscatter of pixels contained within each feature class. The dashed lines are the best-fit models. Model parameters are listed in Table 1. $\langle\sigma_o\rangle$ for empty and ephemeral lakes from region 1 (T39/T55) are over-plotted in black and white, respectively. Note that ephemeral features are initially consistent with the partially filled lake class and later consistent with the empty lake class.

Table 1
Best-fit model parameters for empty and partially filled lake observations. Errors represent 95% confidence intervals. No errors are reported for fits with zero degrees of freedom.

Feature [Number of data points]	QS model	Parameters			
		ϵ_r	θ_{RMS}	A	n[a]
Empty lake class [110]	Gaussian[b]	2.74 ± 0.30	12.88 ± 1.60°	0.55 ± 0.07	1.22
	Hagfors	5.36 ± 1.58	12.56 ± 2.58°	0.41 ± 0.12	1.22
Partially filled lake class [101]	Gaussian[b]	2.09 ± 0.16	15.84 ± 2.00°	0.11 ± 0.02	1.22
	Hagfors	3.49 ± 1.00	15.52 ± 4.52°	0.06 ± 0.04	1.22
Background regions [211]	Gaussian	1.78 ± 0.20	9.01 ± 4.01°	0.38 ± 0.03	1.22
	Hagfors[b]	2.26 ± 0.20	6.18 ± 4.01°	0.34 ± 0.04	1.22
Empty #155 [3]	Gaussian[b]	3.20	16.10°	0.44	1.22
	Hagfors	10.01	5.13°	0.36	1.22
Partially filled #64 [4]	Gaussian[b]	1.78 ± 0.26	8.74 ± 2.90°	0.17 ± 0.10	1.22
	Hagfors	2.18 ± 0.05	6.70 ± 0.44°	0.14 ± 0.01	1.22
Region 1 empty [2]	Gaussian	2.74[a]	9.80°	0.38	1.22
	Hagfors	2.74[a]	9.20°	0.38	1.22
Region 1 background [2]	Gaussian	1.78[a]	14.40°	0.30	1.22
	Hagfors	2.26[a]	9.50°	0.28	1.22
Region 2 empty [2]	Gaussian	2.74[a]	12.0°	0.44	1.22
	Hagfors	2.74[a]	10.9°	0.45	1.22
Region 2 background [2]	Gaussian	1.78[a]	18.2°	0.38	1.22
	Hagfors	2.26[a]	12.6°	0.38	1.22
Empty lakes #34–36 [3]	Gaussian[b]	4.43	18.8°	0.27	1.22
	Hagfors[c]	N/A	N/A	N/A	N/A
Partially filled lake #100 [3]	Gaussian[b]	2.69[a]	20.76°	0.084	1.22
	Hagfors	6.19	19.24°	−0.04	1.22

[a] Denotes that the parameter was held constant during fitting. Dielectric constant (ϵ_r) is held constant for regions 1 and 2 because there are only two independent data points. Cosine power (n) is held constant due to a lack of high incidence angle observations.
[b] Emphasizes models which best fit the dataset. Model preferences are not reported for regions 1 and 2 beacuse there are only two independent data points.
[c] The Hagfors model could not be used to model empty lakes #34–36, as it required non-physical values for the Fresnel reflection coefficient.

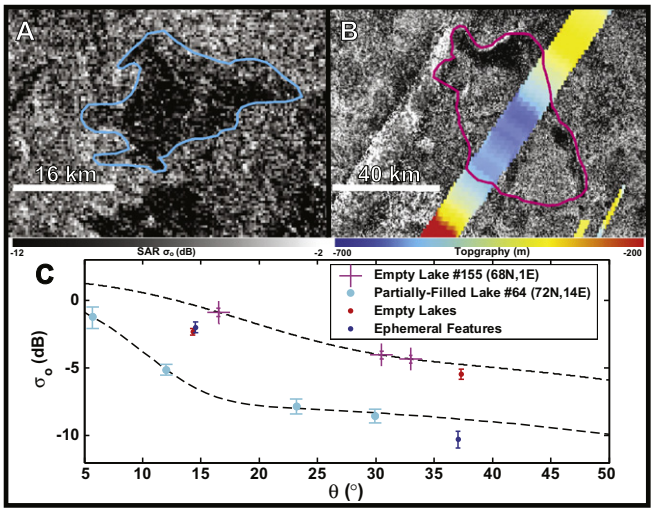

Fig. 2. σ_o variation for a individual partially filled (cyan) and empty (magenta) lakes observed at multiple incidence angles. Images are equicylindrical projections with a logarithmic stretch from −20 dB to 2 dB. (A) Partially filled lake feature (#64). (B) Empty lake feature (#155). (C) Backscatter values for partially filled lake #64 and empty lake #155 with best-fit Gaussian scattering models depicted by dashed black lines. Red and blue dots represent empty lakes and ephemeral features in region 1 (T39/T55). All error bars represent 95% confidence on mean backscatter. Fit parameters are listed in Table 1.

considered may be over-simplified and unrepresentative. Complex scattering effects or multi-layer models, such as subsurface ice cylinders observed in Greenland (Rignot et al., 1993) or Mie scattering from cm-scale cobbles (Le Gall et al., 2010), may be required to explain the low incidence angle behavior of backscatter on Titan. However, deriving a more complex model for radar backscatter of Titan's hydrologic features is beyond the scope of this work. The purpose of backscatter modeling herein is to verify that the observed backscatter variations described in the following sections represent temporal surface change and cannot be explained by variations in incidence, azimuth, or polarization angles (null hypothesis).

3. Observations of change

3.1. South polar region

SAR images of Titan's south polar region were acquired during 10 flybys dating between September 2005 and January 2010 (Table 2). Overlapping coverage is predominantly between two northwest–southeast trending swaths (T36 and T39) and five more recent southwest–northeast trending swaths (T55–T59). Also significant is a west–northwest to east–southeast swath (T49, Fig. 3). The largest baseline for observing potential change among these observations is ~2 years. Additional radar swaths of the south polar region will be obtained during Cassini's Solstice Mission in July 2010 (T71), October 2013 (T95), February 2014 (T98), and July 2016 (T120).

For the majority of overlapping coverage, changes in appearance can be readily explained by variations in observational geometry. Morphologic features including bright hummocky terrain associated with topographic highs (Lopes et al., 2010), dendritic channel networks, and lacustrine features near the pole (70–90°S), appear unchanged (Fig. 3). Persistent lacustrine features include filled lakes in the vicinity of the pole and dark areas, morphologically similar to terrestrial mud-flats (Lopes et al.,

Table 2
South polar SAR swaths between September 2005 and January 2010. H denotes HiSAR (low resolution SAR acquired outside 25 min from closest approach). ISS observations of the south polar region acquired between July 2004 and March 2009 are also included.

Swath	Acquisition date	L_s (°)	Overlapping observations
T07	September 7, 2005	309	T36H
T36	October 2, 2007	337	T49, T55–T59
T39	December 20, 2007	339	T55–T59
T49	December 21, 2008	352	T36
T55	May 21, 2009	357	T36, T39, T56
T56	June 6, 2009	358	T36, T39, T55
T57	June 22, 2009	358	T36, T39, T58
T58	July 8, 2009	359	T36, T39, T57
T59	July 24, 2009	359	T36, T39, T55H
T65	January 12, 2010	5.5	T07, T39, T57–T59
Rev0A (ISS)	July 3, 2004	293	T7–T59
Rev09 (ISS)	June 6, 2005	306	T7–T59
T51 (ISS)	March 27, 2009	355	T7–T59

2010), found near (150°E, 80°S) and (0°E, 75°S). Limited topography from SAR-Topo measurements (Stiles et al., 2009; Zebker et al., 2009) suggests these features are located in the lowest elevations of the south polar region (Fig. 3). When referenced to estimates of Titan's geoid (Iess et al., 2010), these areas have comparable elevations to north polar seas, or mare shorelines reported in Kirk et al. (submitted for publication).

Unambiguous changes in radar reflectivity are observed within three regions on the surface: (60°S, 150°E) and (70°S, 260°E), where ephemeral lacustrine features are observed, and Ontario Lacus, a large lake centered at (72°S, 175°E). In the first two regions, partially filled lake features are observed to transition over time into features morphologically consistent with empty lake basins. Some partially filled features remain radar-dark relative to their surroundings, but show an increase in backscatter that cannot be explained by incidence angle variations using common scattering models. Ontario Lacus shows evidence for shoreline recession between initial ISS observations in July 2004/June 2005 (Turtle et al., 2009) and recent SAR images obtained in July 2009 (Wall et al., 2010). In addition to these observations, the appearance of dark features, interpreted as standing bodies of liquid hydrocarbon, has been previously documented by Cassini's Imaging Science Subsystem (ISS) at Arrakis Planitia between July 2004 and June 2005 (Turtle et al., 2009; Turtle et al., submitted for publication).

3.1.1. Ephemeral lacustrine features

Ephemeral lacustrine features with areas of ~100 km^2 were observed in two portions of Titan's south polar terrain. SAR images of Region 1 (63–58°S, 144–153°E) were obtained in December 2007

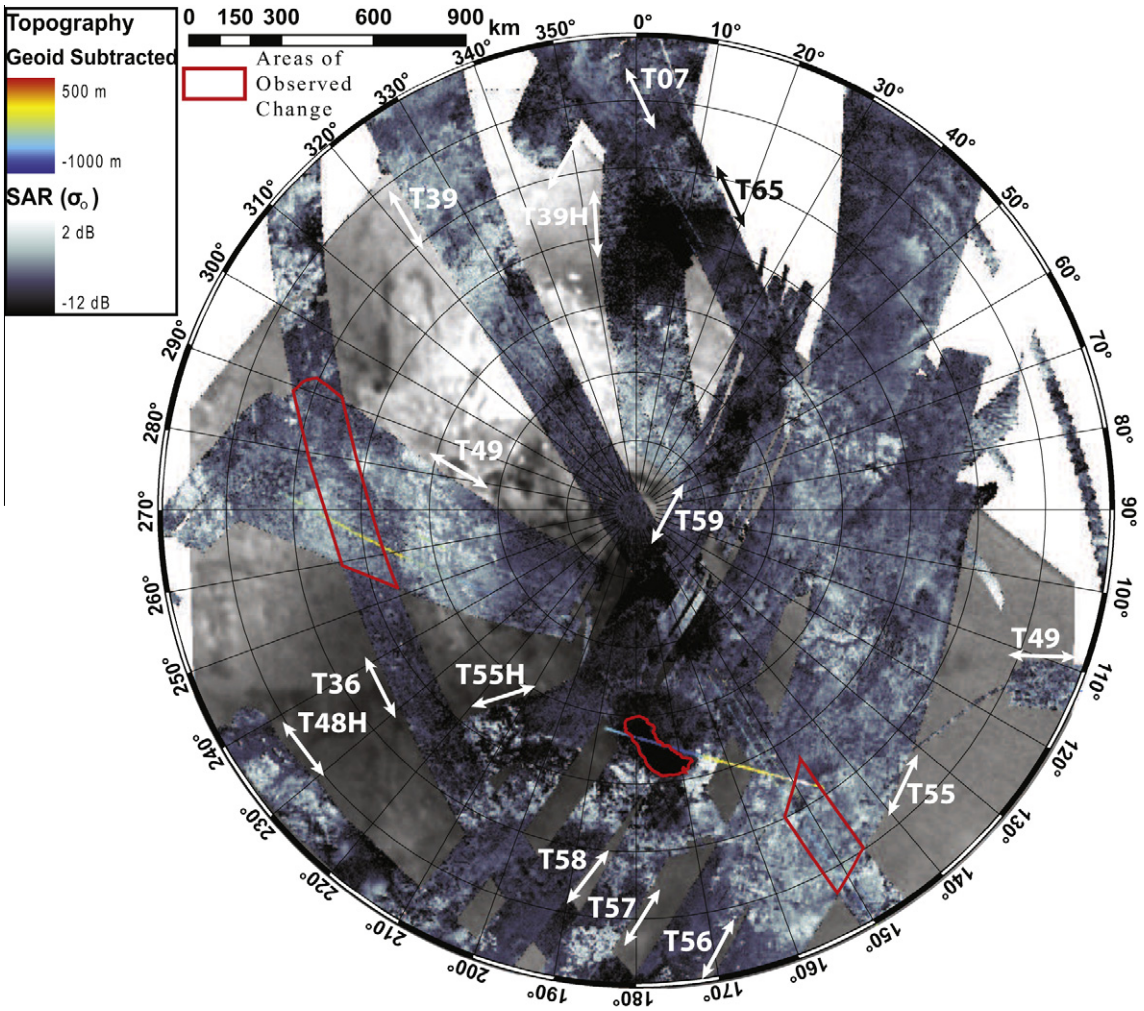

Fig. 3. SAR mosaic of Titan's south polar region (90–55°S) for September 2005 through January 2010 (TA-T65). SAR data has been noise subtracted and corrected for bulk incidence angle effects. The June 2005 (Rev09) ISS observation is used as a background. The three areas which include ephemeral features are outlined in red. Geoid-subtracted topography is overlayed using the depicted colormap.

(T39) and May 2009 (T55) (Fig. 4A–C). In general, the T39 SAR image shows lower σ_o values than T55, likely associated with the higher incidence angle for this pass. A collection of features which have morphologies consistent with hydrologic origin, however, have a significantly lower σ_o as compared to their surroundings. In the area of interest, the incidence angles for T39 and T55 are ~37° (32–41°) and ~14° (11–18°), respectively. The look direction azimuths vary by 160° and the electric field vector of the incident wave was within 20° of horizontal polarization. The ratio between the backscatter cross-section of ephemeral features in T55 vs. T39

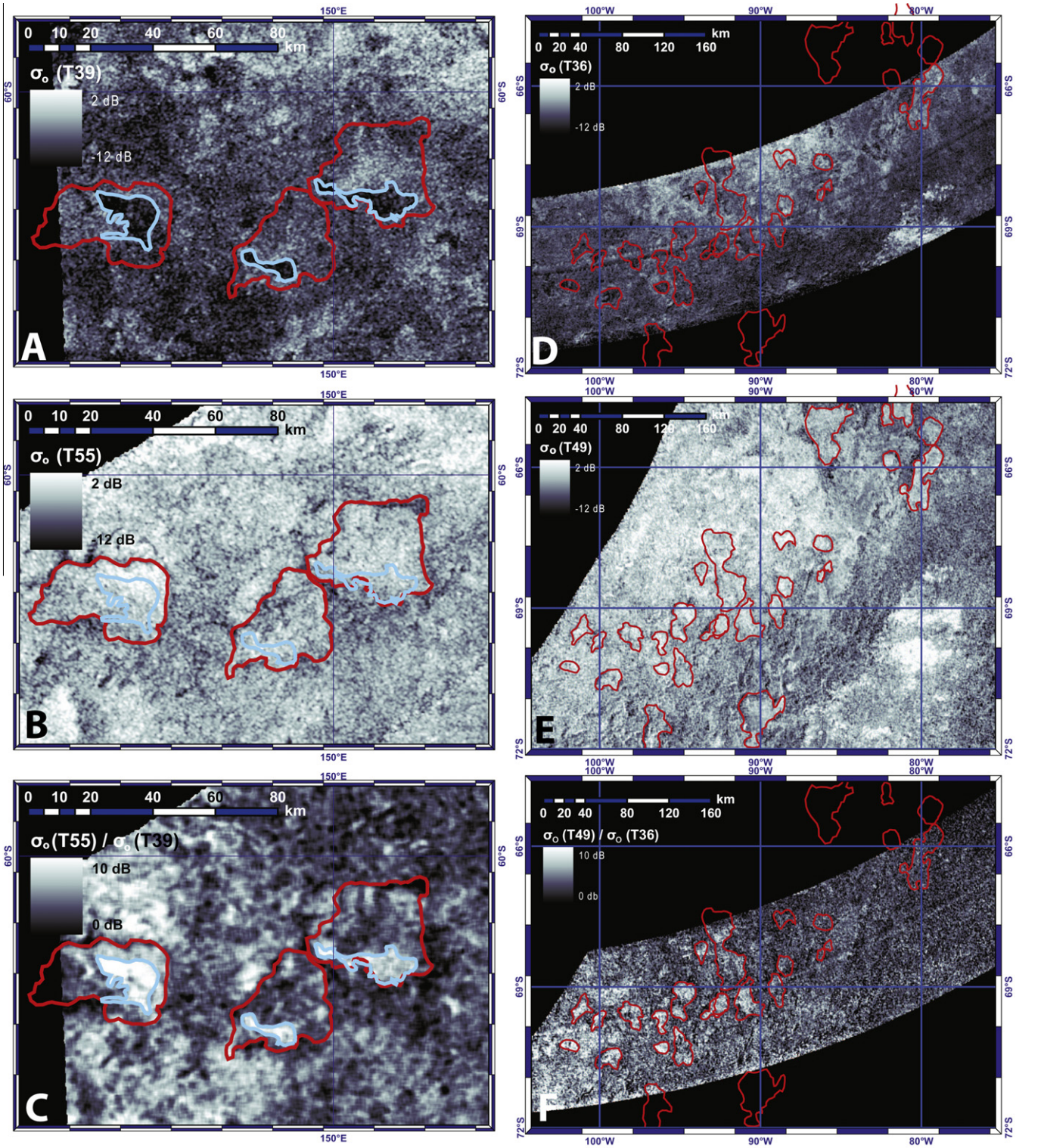

Fig. 4. Ephemeral observations. The left hand column shows images of region 1 while the right hand column shows images of region 2 (Section 3.1.1); (A) T39; (B) T55; (C) σ_o ratio of T55/T39; (D) T36; (E) T49; (F) σ_o ratio of T49/T36; SAR images are displayed from −12 dB to 2 dB. Ratio images are displayed from 0 dB to 10 dB. Lacustrine features are outlined in red. Partially filled lakes in T39 are outlined in cyan. Full resolution versions of these images are available in the Supplementary material. (For interpretation of the references to color in this figure legend, the reader is referred to the web version of this article.)

is 6–10, while the ratios for most other features in the image are 1.5–4 (Fig. 4C). A purely diffuse cosine scattering law would produce a ratio of 1.26 for a cosine power of 1.22, suggesting that there is a strong non-diffusive component in σ_o for the observed areas, which is consistent with observations of other surfaces on Titan (Wye et al., 2008). Table 3 lists the average σ_o and incidence, azimuth, and polarization angles within the outlined features (Fig. 4A and B). The three dark features in T39 (outlined in cyan in Fig. 4A) are nested within empty lake features (outlined in red) and have morphologic borders with similar complexity to partially filled lakes. In T55 (Fig. 4B) the boundary between the previously dark features and the surrounding empty lake basins has disappeared, supporting the case that temporal surface change has taken place. Moreover, this argues that the change is such that the lake interior transitioned to resemble the surrounding terrain, as would be expected if the lake drained or evaporated. Other areas in the study region are dark in both observations, but show similar variation in backscatter between passes. These features are consistent with partially filled lakes whose liquid levels have changed (Section 3.1.2).

Region 2, located further south from the T39/T55 overlap area (72–63°S, 252–290°E), also shows large backscatter variations in lacustrine features (Fig. 4D–F). This area was first imaged in early October 2007 (T36) and then in late December 2008 (T49), providing a 1.25 year baseline. The differences in look direction azimuth and polarization angle are 60° and 25°, respectively. The backscatter and observational geometry of this study region is similar to the T39/T55 observations. Incidence angles for T36 and T49 are ~35° (30–40°) and ~13° (10–24°), respectively, and the ratios of backscatter cross-sections of the background and ephemeral features in T36 vs. T49 range from 1.5 to 4 and 6 to 11 (Fig. 4F). The area of change is limited to the western section of the overlap area between 252°E and 270°E. The brightening of empty lake features in the eastern half of the overlap region is indistinguishable from the brightening of the background, since both are explained by incidence angle variations. The absolute σ_o values for bright features in the eastern half of the overlap region are higher than their western counterparts in T36, but similar in T49, consistent with the presence of an attenuating liquid layer in the western T36 features that was not present in the T49 observations. The variations in incidence angle between the western and eastern lake features within T36 is less than 4°, too small to account for the σ_o differences if backscatter from these features is similar to empty or partially filled lake basins observed in other areas of Titan (Section 2).

The quasi-specular plus diffuse model presented in Section 2 for classes of empty and partially filled lakes cannot be used to describe the backscatter variations in the ephemeral features located in Regions 1 and 2 without modifying the model coefficients between observations. In the absence of surface change, incidence angle variation would produce a backscatter ratio of ~1.3 between observations, assuming a diffuse scattering law with a cosine power of $n = 1.22$. While the quasi-specular component preferentially increases backscatter at low incidence angles, the combined model cannot reproduce the ratio of $\geqslant 6$ observed for the ephemeral features without increasing the amplitude of the diffusive component of later observations. The required increase would need to be roughly a factor of 3 for the mean of the return from the dark features, and a factor of 10 for the lowest backscatter values found within the features. The quasi-specular plus diffuse model can, however, be used to explain the non-ephemeral and background backscatter using parameters similar to those for the empty and partially filled lake classes (Fig. 5).

The initial σ_o values for the ephemeral features in both areas of change (T36 and T39) fall within the class of partially filled lakes. Later observations of some ephemeral features (T55 and T49), along with the non-ephemeral features, fall within the class of empty lakes. Other ephemeral features, which have similar relative backscatter variation between observations, remain dark relative to their surroundings. This is consistent with these features remaining partially filled, although with a lower liquid level. Some backscatter models, such as a small perturbation model (Rice, 1951) for Bragg wave backscatter using the empirical Pierson–Moskowitz wave power spectrum (Pierson and Moskowitz, 1964), can match the backscatter curves for some of the ephemeral features. These models, however, require significant surface roughness on the liquid and would present backscatter functions which cross between the empty and partially filled lake classes. None of the features observed on Titan have such scattering properties, including lakes observed at multiple incidence angles (Fig. 2).

Several arguments oppose simple surface scattering as the cause for ephemeral feature backscatter. Scattering models which fit the ephemeral features forbid a significant diffuse component and would require a highly variable surface environment over short length scales as, in each region, transitions are observed from partially filled to both partially filled and empty lake classes. In

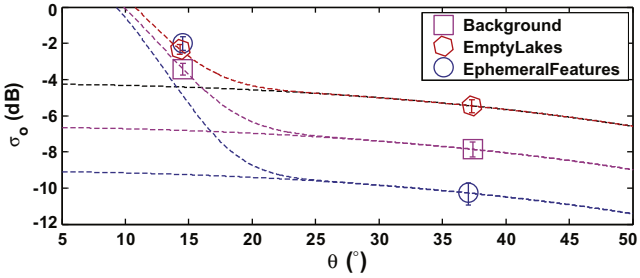

Fig. 5. σ_o values for the ephemeral features in region 1 (T39/T55). Fit parameters are listed in Table 1.

Table 3
Ephemeral feature $\langle\sigma_o\rangle$ values and observational geometries. Ephemeral features refer to partially filled to empty lake transitions while partially filled features correspond to changes in lake depth without complete drying. Incidence angles are measured from the local surface normal. Azimuth angles are measured counter-clockwise positive from east. Polarization angles represent the angle between the electric field vector and the plane of incidence, measured counter-clockwise positive from perpendicular (horizontal polarization) when looking down the wave vector. Error bars in $\langle\sigma_o\rangle$ represent 95% confidence intervals (CI) obtained using a boot-strap Monte Carlo technique as described in Press et al. (1992).

Swaths		Feature	Incidence angle (°)		Azimuth angle (°)		Polarization angle (°)		$\langle\sigma_o\rangle$ (dB)	
T39	T55	Background	36.8	14.2	165	320	195	177	−7.86 ± 0.44	−3.43 ± 0.34
T39	T55	Empty lake	38.8	14.4	166	328	199	170	−5.46 ± 0.38	−2.33 ± 0.27
T39	T55	Ephemeral	37.4	14.3	166	327	197	170	−10.27 ± 0.66	−1.24 ± 0.34
T39	T55	Partially filled	36.5	18.6	166	327	196	175	−13.00 ± 0.39	−5.70 ± 0.28
T36	T49	Background	33.0	21.4	316	20	159	140	−6.50 ± 0.41	−3.10 ± 0.24
T36	T49	Empty lake	34.0	17.3	308	10	165	140	−4.60 ± 0.32	−2.20 ± 0.20
T36	T49	Ephemeral	35.7	13.0	293	6	166	142	−8.00 ± 0.67	−0.80 ± 0.45
T36	T49	Partially filled	34.2	13.2	302	8	163	142	−12.0 ± 0.90	−5.10 ± 0.33

addition, surface waves on the lake do not naturally explain transient morphologic boundaries and are inconsistent with backscatter variations of other filled or partially filled lakes observed at multiple incidence angles. While the wave power spectrum and wave–wind interaction properties of liquid hydrocarbon on Titan are not well understood, the root-mean-square (RMS) wave height required to reproduce the ephemeral backscatter variations is ~9 mm using parameters defined in Pierson and Moskowitz (1964), larger than the 3 mm RMS height limitation imposed on Ontario Lacus roughness by recent radar data (Wye et al., 2009). Atmospheric scaling arguments suggest that the threshold wind speed required to produce capillary waves in liquid hydrocarbon is ~0.5–1 m/s (Lorenz et al., 2010b). For the planetocentric solar longitude (L_s) range of ephemeral feature observations ($337° \leqslant L_s \leqslant 359°$), global circulation model (GCM) estimations of wind speed remain below this threshold (Lorenz et al., 2010b). In addition, average σ_o decreases with lake size (Paillou et al., 2008b), consistent with a rough lakebed contributing to backscatter in an environment where larger lakes are deeper. If backscatter from surface waves were primarily responsible for lake σ_o, larger lakes with greater fetch would produce bigger waves and greater off-nadir backscatter (Lorenz et al., 2010b).

The Cassini RADAR is linearly polarized and the electric field vector is oriented approximately parallel to Titan's surface during SAR operation. Deviations from horizontal polarization are less than 40° for the areas studied and polarization effects are not expected to produce significant changes in observed backscatter. In quasi-specular facet scattering, where contributing surface elements are assumed to be oriented perpendicular to the illumination direction, and coherent diffuse scattering polarization effects are negligible. In non-coherent diffuse backscatter, polarization is randomized. For multiple scattering and wavelength-scale rough surfaces, where polarization effects can be important, the maximum potential change in reflected energy between observations from polarization effects alone is 16% for region 1 and 45% for region 2. These maxima, which are far less than the observed tenfold change in backscatter, occur when there is no return for parallel polarization, such as would be the case for a corner reflector oriented at the Brewster angle. Empirically, there are no obvious correlations between polarization angle and backscatter cross-section in SAR images of Titan's polar regions.

Observed σ_o values for the empty lake features in regions 1 and 2 are consistent with the σ_o values for all empty lakes observed to date. The σ_o values for ephemeral features in regions 1 and 2 are initially consistent with partially filled lake backscatter and a year later consistent with empty lake returns. Ephemeral features are inconsistent with the presented model using constant coefficients. Explaining them using incidence angle variations requires backscatter behavior not observed on Titan. Polarization and azimuth angle effects alone cannot explain the differences. Coupling these radiometric arguments to the transient borders between the ephemeral observations supports the conclusion that temporal change has taken place. The most probable candidate for this surface change is a reduction in the liquid level of partially filled lakes. In the next section, a two-layer model is developed to estimate the liquid level reduction required to explain observed backscatter variations.

3.1.2. Two-layer model

In order to understand the ephemeral lake features observed in the south polar region, we use a simple two-layer model to estimate the ratio between partially filled ($\sigma_{o,\ \mathrm{fil}}$) and empty ($\sigma_{o,\ \mathrm{emp}}$) lake backscatter, deriving a lower limit on liquid depth changes from radar returns:

$$\sigma_{o,\ \mathrm{fil}} = T_\perp(\theta)T_\perp(\theta_{\mathrm{liq}})A^2(\theta_{\mathrm{liq}},\Delta d)\frac{\sigma_{o,\ \mathrm{bed}}(\theta_{\mathrm{liq}},n_{\mathrm{liq}})}{\sigma_{o,\ \mathrm{bed}}(\theta_{\mathrm{atm}},n_{\mathrm{atm}})}\sigma_{o,\ \mathrm{emp}} \quad (4)$$

where $T_\perp(\theta)$ is the Fresnel transmission coefficient for perpendicular polarization, $A(\theta_{\mathrm{liq}}, \Delta d)$ is the attenuation coefficient, $\sigma_{o,\ \mathrm{bed}}(\theta_{\mathrm{liq}}, n_{\mathrm{liq}})$ is the interaction with the lake floor in the liquid medium, and $\sigma_{o,\ \mathrm{bed}}(\theta_{\mathrm{atm}}, n_{\mathrm{atm}})$ is the empirical backscatter function for exposed lakebeds. This model consists of three main components (Fig. 6): signal interaction with the liquid surface, attenuation through the liquid layer, and interaction with the lake bottom. For the purposes of this work, the liquid surface was assumed to be smooth at the radar wavelength, allowing wave transmission to be determined by the Fresnel transmission for an interface between atmosphere ($n_{\mathrm{atm}} \sim 1$) and liquid hydrocarbon ($n_{\mathrm{liq}} \sim 1.3$). The real part of the index of refraction for liquid hydrocarbon was derived from the dielectric constant measurement of $\epsilon_r = 1.75$ performed by Paillou et al. (2008b) using liquid natural gas (LNG). Any additional backscatter from the liquid surface would tend to decrease the percentage of transmitted radiation and increase the calculated depth change. Attenuation is calculated using the attenuation coefficient for a complex medium:

$$A(\theta_{\mathrm{liq}}) = e^{-4\pi\kappa\Delta d\sec\theta_{\mathrm{liq}}/\lambda} \quad (5)$$

where θ_{liq} is the incidence angle within the liquid medium from Snell's law, λ is the free-space SAR wavelength, κ is the imaginary component of the complex index of refraction, and Δd is the change in depth of the liquid layer.

The difference in lakebed backscatter between filled and empty states results from a brightening associated with the decreased incidence angle (θ_{liq} vs. θ_{atm}) at the liquid interface, and a potential darkening from decreased dielectric contrast ($\epsilon_{\mathrm{liq}}/\epsilon_{\mathrm{bed}}$ vs. $\epsilon_{\mathrm{atm}}/\epsilon_{\mathrm{bed}}$) at the lakebed interface. The importance of the decreased dielectric contrast can vary. For a diffusely scattering lakebed with a saturated subsurface the effect would be small. For a completely dry lakebed, however, the effect can be large. In the case of an impermeable lakebed surface, the backscatter decrease would approximate the ratio of the normal-incidence Fresnel reflection coefficients for quasi-specular facet scattering. For surface dielectric constants varying between water–ice ($\epsilon_r = 3.16$) and tholin ($\epsilon_r = 2.0$–2.4), the reduction in the reflection coefficient is between a factor of 3 and 10. For the case of a permeable lakebed, the effect of the decreased dielectric contrast is difficult to model because of the unknown nature of Titan's regolith structure. In the simplest model for a diffusely scattering lakebed, Mie theory can be used to approximate an ensemble of irregular scatterers which are on the order of, or smaller than, the wavelength (Black et al., 2001; Pollack and Cuzzi, 1980). For this scenario, backscatter reductions

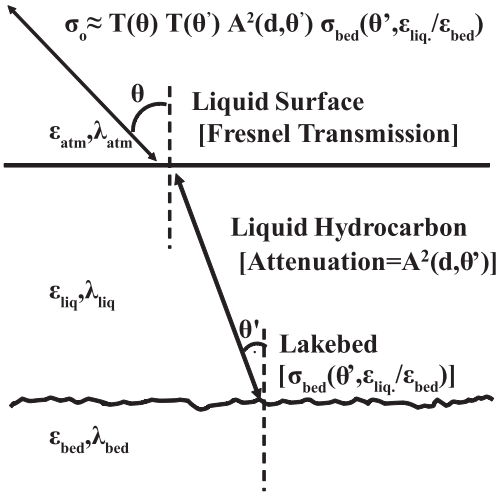

Fig. 6. Schematic of two-layer model.

are similar in magnitude to those modeled by the Fresnel reflection coefficient. However Mie theory, which usually refers to non-interacting separable particles, has limited use when applied to dense aggregates such as planetary regoliths. The effect we are discussing, namely a change in radar reflectivity between saturated vs. unsaturated regolith, is a well known terrestrial phenomenon. For liquid water on Earth, which has an index of refraction of $(76 - 2.3i)$ at a wavelength of 2.2 cm and ambient conditions (Barthel and Buchner, 1991), soil moisture can increase (as opposed to decrease, as would occur on Titan) σ_o by a factor of ~5 for volumetric water content of 0.6 g/cm^3 (Dobson et al., 1985). When calculating liquid depth variations using the two-layer model, we neglect the decreased dielectric contrast and provide a constraint on the maximum liquid depth. However, as shown below, there is evidence that the measurements of relative liquid depth are robust with respect to this effect.

If permeable, the pore space below a filled lake will contain liquid hydrocarbon, saturating the regolith (Hayes et al., 2008). This saturated medium can take decades to centuries to radially flow away from the lake (Section 4). If the liquid in the lake is removed, evaporation from the saturated regolith will proceed more slowly than for the exposed lake, limited by the diffusivity and permeability of the porous medium (Saravanapavan, 2000). It is therefore possible for the regolith below an empty lakebed to remain saturated for some time after the lake itself has evaporated. In this case the subsurface scattering component of the radar return will not be strongly affected by decreased dielectric contrast at the lakebed interface. The lack of a significant increase in σ_o just outside of the near-shore region of Ontario Lacus (Section 3.1.3), where a shallow regional slope provides a gradual transition between saturated and potentially unsaturated regolith, is consistent with this hypothesis.

As discussed above, Fig. 2 shows the backscatter variation for an empty and a partially filled lake observed at multiple incidence angles. Both features were located in the north polar region and observed during northern winter, when minimal evaporation and precipitation are expected (Mitchell, 2008; Newman et al., 2008; Graves et al., in preparation). Backscatter models for the σ_o variations in these two observations show that the partially filled lake has a more pronounced dependence on low-angle incidence as compared to empty-lake backscatter, consistent with the increased incidence angle within the liquid medium. The overall lower σ_o values are consistent with attenuation through a liquid layer. The collective set of empty and filled lake σ_o values (Fig. 1) also shows steeper incidence dependence for the partially filled lakes at low angles. Arguably, the inflection point between quasi-specular and diffuse scattering exists at ~20° in the empty lake class and ~30° in the partially filled lake class (Fig. 1). If these inflection points indeed both represent the transition between quasi-specular and diffuse backscatter at the lakebed interface, then that suggests an incidence angle shift due to Snell's Law for an overlying medium with a real dielectric constant of ~2, consistent with liquid hydrocarbon.

The best-fit model for the partially filled lake class is similar to the best-fit model for the empty lake class modified by the assumptions of the two-layer model presented above (Fig. 7). After evaluating the empty-lake backscatter at θ_{liq} and multiplying by the transmission and attenuation (Eq. (5)) coefficients, using a best-fit depth of 1.2 m, the shape and magnitude of the resulting backscatter is very similar to the partially filled lake class. We did not account for the effect of decreased dielectric contrast at the lakebed interface, but it is indistinguishable from liquid attenuation in this model. Simply multiplying the empty-lake backscatter by a constant attenuation factor also produces a similar result, although it does not match the shape of the profile as well at low incidence angles (Fig. 7). Overall, the backscatter functions observed for both single features and the collective set of empty and partially filled lakes is consistent with the presented two-layer model.

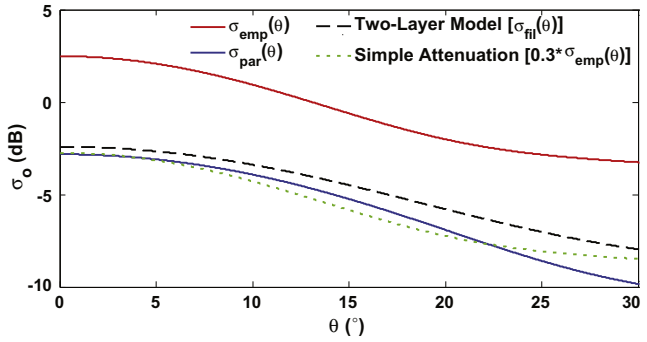

Fig. 7. Best-fit backscatter models for empty (red) and partially filled (blue) lake classes. The black dashed line represents the empty-lake backscatter modified by the two-layer model (Eq. (4)) and the green dotted line is the empty-lake backscatter multiplied by a constant attenuation factor. (For interpretation of the references to color in this figure legend, the reader is referred to the web version of this article.)

Changes in lake depth can be calculated from the backscatter ratio of subsequent observations using Eq. (4) for partially filled to empty lake transitions and Eq. (5) for lakes which remain partially filled, as a liquid layer is present in both observations. In both cases, the calculated liquid depth is inversely proportional to the complex index of refraction or loss tangent of the liquid. Ignoring the possible affects of the decreased dielectric contrast, we calculate $\sigma_{o,\,bed}(\theta_{liq}, n_{liq})/\sigma_{bed}(\theta, n_{atm})$ using best-fit Gaussian scattering model through the observed empty-lake backscatter. Typical values for $30° < \theta < 40°$, where the ephemeral lakes are observed, are ~1.2 and do not vary significantly. The brightening effect is more apparent for lower incidence angles, where $\sigma_{o,\,bed}(\theta_{liq})/\sigma_{bed}(\theta_{atm})$ can grow up to a factor of 3 for a realistic parameter space. However, the observational geometry of ephemeral features is such that the earlier observations (T36 and T39) were acquired at larger incidence, where the brightening effect is less significant. For incidence angles less than 40°, $T(\theta)$ varies from 98% to 100% for parallel polarization and 96% to 98% for perpendicular polarization. Thus, reflection loss at the atmosphere/liquid interface is minimal. In the model, the dominant term, by roughly an order of magnitude, is the observed value $\sigma_{o,\,fil}/\sigma_{o,\,emp}$.

Using the average σ_o values listed in Table 3 and a loss tangent of $\tan\Delta = (9.2^{+2.5}_{-2.0}) \times 10^{-4}$ (Hayes et al., in press; Paillou et al., 2008a) Eqs. (4) and (5) yield depths of 0.7–1.0 m for ephemeral lake depths in the T39/T55 and T36/T49 overlap areas. These values are consistent for both partially filled to partially filled and partially filled to empty lake transitions. The effect of a decreased dielectric contrast at the lakebed interface could decrease estimated depth changes, but Ontario Lacus and other potentially shallow liquid basins do not show the significant increase in σ_o just outside the lake that would be expected in this scenario. Additionally, consistency between partially filled to partially filled and partially filled to empty lakes transitions would not be expected if the affect of the decreased dielectric contrast were significant. We list model results for each ephemeral lake region and transition type in Table 4. As we will see in the following section, model results agree with the estimated reduction in the depth of Ontario Lacus from shoreline recession measurements.

3.1.3. Ontario Lacus [72°S, 175°E]

Ontario Lacus, with a surface area of 15,600 km^2 as of July 2009, is the largest lacustrine feature in the south polar region. It is interpreted as a liquid hydrocarbon lake and was originally observed by

Table 4
Two-layer model loss rate results for ephemeral lake features. Modeled depth change and flux rates are proportional to $\frac{(9.2\times10^{-4})}{\tan\Delta}$.

Swaths		Transition	Modeled depth change (m)	Flux (m/year)
T39	T55	Partially filled to empty	1.00 ± 0.33	0.71 ± 0.23
T39	T55	Partially filled to partially filled	0.98 ± 0.26	0.69 ± 0.19
T36	T49	Partially filled to empty	0.74 ± 0.30	0.61 ± 0.24
T36	T49	Partially filled to partially filled	0.78 ± 0.38	0.64 ± 0.31

ISS in July 2004 and June 2005 (Turtle et al., 2009). Subsequent observations by the Visual and Infrared Mapping Spectrometer (VIMS) in December 2007 demonstrated liquid ethane was present in the lake (Brown et al., 2008). Additional analysis of VIMS data led to the identification of annuli surrounding the feature that Barnes et al. (2009) interpreted as past shorelines. Recent RADAR data of Ontario Lacus have been acquired in the form of altimetry measurements in December 2008 (T49) and SAR images in June 2009 (T57), July 2009 (T58), and January 2010 (T65) (Wall et al., 2010). The altimetry measurements show that the lake surface was smooth and specular during the T49 flyby, with a RMS height variation of less than 3 mm over the 100 m Fresnel zone of the radar footprints (Wye et al., 2009). SAR imagery shows Ontario Lacus as a complex feature with multiple inlets, shoreline features, and contributing channel networks (Wall et al., 2010). Lorenz et al. (2010a) discuss morphologic similarities between Ontario and the transient lake at Racetrack Playa, Death Valley National Park, CA, USA.

Comparison between the June 2005 ISS and July 2009 SAR data shows a difference in the shorelines of Ontario (Fig. 8). While the northern borders match within the ~1 km resolution of the ISS data (Turtle et al., 2009), the southern borders show up to a 20 km recession of the shoreline between ISS and RADAR images. While registration accuracy (2 km RMS) between the datasets is sufficient to support the interpretation of temporal surface change additional ISS data, obtained in March 2009 (T51) at a resolution of ~5 km, confirm the observed shoreline recession at the southernmost end of the lake (Turtle et al., submitted for publication). Furthermore, the 2009 ISS shoreline matches the 2009 SAR shoreline to within the expected registration error (Turtle et al., submitted for publication). Lastly, the 2005 ISS border roughly correlates with a narrow bright rim observed in the SAR data (Fig. 8) (Wall et al., 2010). This rim is consistent with a previous shoreline and approximately coincides with the annuli observed by Barnes et al. (2009) using VIMS.

Although cross-instrument comparisons can be awkward, there are several lines of evidence that support the interpretation of shoreline recession at Ontario Lacus. First, as stated above, the shorelines at the northern-most end of the lake match to within the limits of ISS resolution, while there is a ~10 km recession in the southwest corner. Second, altimetry measurements obtained in December 2008 (T49) show that there is a consistent slope for 100 km leading up to the southeast corner of the lake (Fig. 9). At the resolution of the available data, there is no break in slope or bench in the topography that could support a vast expanse of mm-deep liquid which would be transparent to radar and opaque to ISS. Third, the two-way dispersion length, or *e*-folding attenuation depth, of the near-shore liquid in Ontario is ~1 m (Hayes et al., in press; Paillou et al., 2008a), suggesting that cross-instrument comparison can, at most, account for ~25% of the observed four meter depth change in Ontario (see below). The average loss rate of ~1 m/year is also consistent with depth changes derived from backscatter modeling of nearby ephemeral lacustrine features. Lastly, there is no significant change in σ_o for pixels outside the 2005 ISS shoreline in the 2009 SAR image. If ISS observed a saturated mud-flat around Ontario, one might expect it to be distinguishable from dry regolith based on the difference in dielectric contrast between saturated and unsaturated pore space (see previous section). Combined with the 2009 ISS observations of Ontario described in Turtle et al. (submitted for publication), these

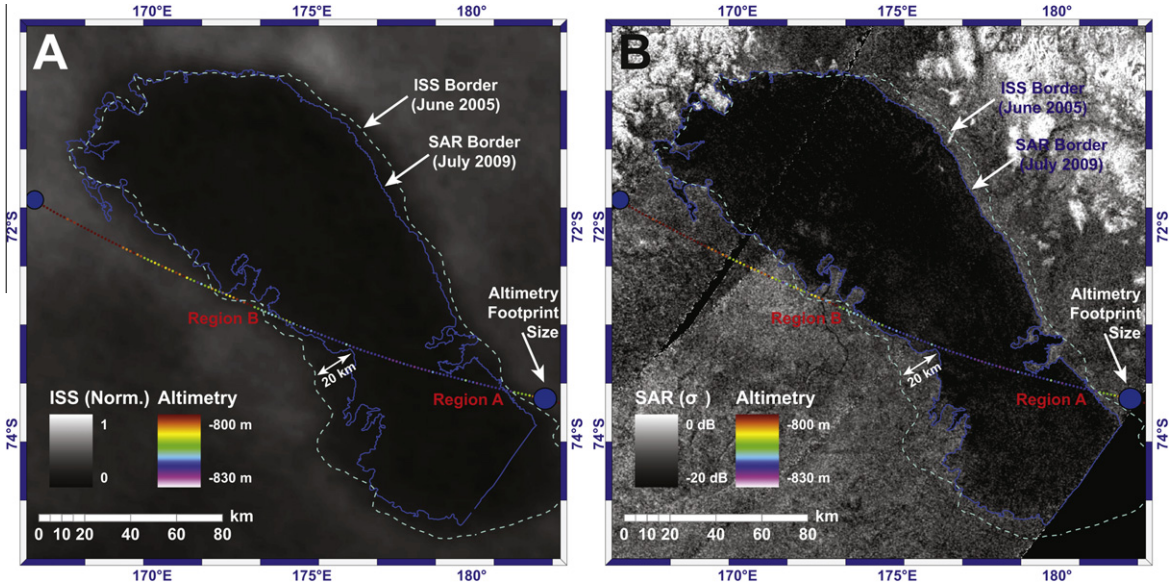

Fig. 8. Equidistant cylindrical projection of of Ontario Lacus. The lake border from the 2005 ISS image is shown in cyan, while the 2009 SAR border is blue. T49 altimetry data is overlain. Heights are calculated from echo center-of-mass and referenced to Titan's geoid as presented in Iess et al. (2010). Altimetry footprint size is shown using blue circles. (A) ISS image obtained in June 2005 (Rev09). ISS shoreline is defined by following a constant contour of relative brightness referenced to local off-shore pixel intensity. (B) SAR image obtained in June and July 2009 (T57/T58).

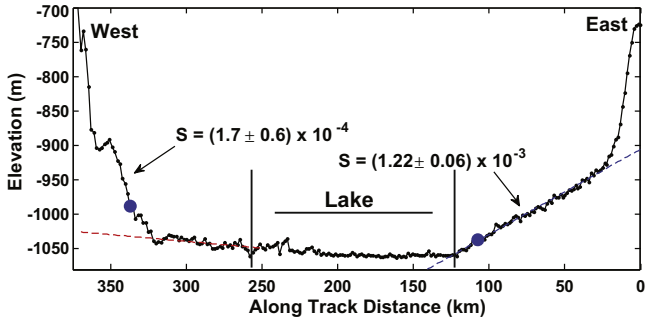

Fig. 9. Analysis of December 2008 (T49) altimetry track. Blue circles correspond to positions marked in Fig. 8. Values represent geoid subtracted altimetry using radar echo center-of-mass. Geoid values obtained from Iess et al. (2010). Local slopes (S) near altimetry intersections with Ontario Lacus are shown in blue (region A) and red (region B). Local slopes are converted to topographic slopes (D) assuming the direction of steepest descent is towards the shoreline (Hayes et al., in press). (For interpretation of the references to color in this figure legend, the reader is referred to the web version of this article.)

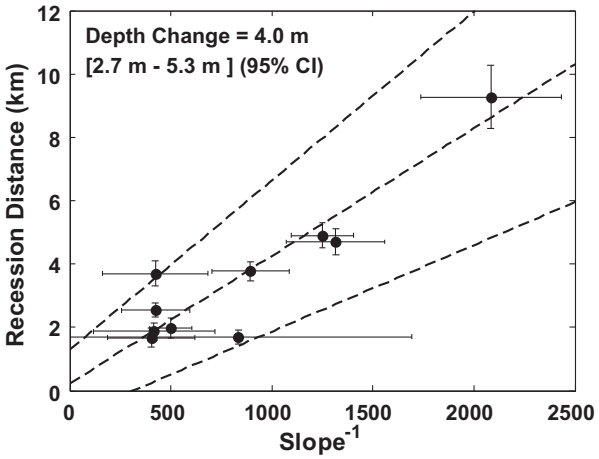

Fig. 10. Scatter plot of recession distance vs. inverse bathymetry slope of Ontario Lacus. Bathymetry values were obtained in 10 areas around the lake by fitting the exponential attenuation of near-shore backscatter. A detailed description of these calculations can be found in Hayes et al. (in press). Errors represent 95% confidence intervals (CI) and the dashed lines are the best fit and 95% CI for a linear fit.

arguments make a compelling case in support of lateral shoreline regression over the observed period.

The average backscatter cross-section ($\langle\sigma_o\rangle$) within Ontario Lacus is approximately equal to the average noise equivalent backscatter ($\sigma_{o,\ ne} = -20 \pm 1$ dB). However, the average backscatter in the southwest portion of the lake, where the largest shoreline recession is observed, is above this noise floor and yields $\langle\sigma_o\rangle = -14 \pm 2$ dB. At an incidence angle of 30° (geometry of T58 near Ontario), a normalized backscatter cross-section of -14 ± 2 dB is consistent with the backscatter from the class of partially filled lakes, suggesting that Ontario Lacus is shallow enough in this region for the RADAR to penetrate the liquid layer (Hayes et al., 2008, in press; Paillou et al., 2008a). Around the entire lake, near-shore $\langle\sigma_o\rangle$ values are also consistent with partially filled lake backscatter and observed to exponentially decrease in the offshore direction (Hayes et al., in press). In Hayes et al. (in press) we use the exponential decay of $\langle\sigma_o\rangle$ as a function of distance from the shoreline to derive relative near-shore bathymetry slopes in different regions around Ontario. When coupled to nadir-looking altimetry measurements obtained in December 2008, these relative slopes can be used to generate a near-shore bathymetry map and derive a value for the imaginary component of the liquid's complex index of refraction ($n + i\kappa$) of $\kappa = (6.1^{+1.7}_{-1.3}) \times 10^{-4}$. The relative differences in lake bathymetry derived in Hayes et al. (in press) correlate with the relative differences in shoreline recession observed between the 2004 and 2009 observations of Ontario, further supporting an interpretation of uniform reduction in lake depth (Fig. 10).

The areal difference between the 2005 ISS and 2009 SAR borders of Ontario Lacus is 3200 ± 200 km^2. In region A (Fig. 8) the average shoreline recession is 2.0 ± 0.2 km. Using a topographic slope $D_A = (2 \pm 0.1) \times 10^{-3}$ (Hayes et al., in press), this recession distance corresponds to a vertical elevation of 4.0 ± 0.5 m. In region B, where $D_B = (1 \pm 0.6) \times 10^{-3}$ (Hayes et al. (in press)) and shoreline recession is 3.8 ± 0.2 km, the resulting elevation change is 3.8 ± 2.6 m. Using the near-shore bathymetry map derived in Hayes et al. (in press), shoreline recession in all regions suggests an average depth change of 4.0 ± 1.3 m (Fig. 10). This average value is consistent with the local results derived in regions A and B using direct altimetry measurements. When comparing recession magnitude to local near-shore slope, shoreline position is determined by examination of average backscatter vs. depth and selecting the region where the exponential decay transitions into shoreline backscatter. The slope of a plot of inverse near-shore bathymetry vs. shoreline recession is the depth change, $\Delta d = 4.0 \pm 1.3$ m, and the offset, $d_{off} = 0.2 \pm 1.2$ m, is consistent with zero (Fig. 10). To within errors, these three estimates are equivalent and suggest an average loss rate of 1.0 ± 0.3 m/year during the 4 years between observations. Using an area of 18,700 km^2 for Ontario in 2005, this loss rate corresponds to 19 ± 6 km^3/year and $(7.9 \pm 2.6) \times 10^{12}$ kg/year assuming the removed material is liquid methane.

Changes in tidal acceleration from Saturn during Titan's 16 day orbital period may affect the shoreline of Ontario. To first order in R_T/a_T, where R_T is Titan's radius and a_T is its semi-major axis, the tangential tidal acceleration (f), assuming Titan acts as a rigid sphere, is (Lorenz, 1994):

$$f = (3/2)GM_sR_T\left[a_T\frac{(1-e_T^2)}{(1+e_T\cos\nu_{TA})}\right]^{-3}\sin 2\phi \quad (6)$$

where G is the gravitational constant, M_s is the mass of Saturn, e_T is Titan's eccentricity, ν_{TA} is Titan's true anomaly, and ϕ is the Titanocentric angle between the sub-Saturn point (0°E, 0°S) and Ontario Lacus (175°E, 72°S). The vertical deviation of the local equipotential surface is $d_{tide} = R_{lake}f/g_T$ (Lorenz, 1994), where g_T is Titan's gravitational acceleration and R_{lake} is Ontario's north–south radius (~125 km). Tidal forcing on Titan is slow enough that there is no resonant amplification of the tides (Lorenz, 1994). For the 2005 ISS (Rev09) and 2009 Radar (T57/T58) observations Titan's true anomaly was 277° and 146°, respectively. The corresponding vertical change in the extremes of the shoreline is ~0.4 m, smaller than the observed 4.0 ± 1.3 m depth change. This tidal amplitude is similar to that reported by Barnes et al. (2009). In addition, shoreline recession measurements suggest a constant depth change around the lake while tidally induced changes would vary in magnitude with north–south distance from Ontario's center-of-mass. We therefore conclude that the tide is not a dominant contributor to the observed change.

The chemical composition of lakes on Titan is expected to be a mixture of ethane, methane, and propane, with trace amounts of higher order hydrocarbons and nitriles (Cordier et al., 2009). At 92 K, methane is greater than four orders of magnitude more volatile than ethane and propane, suggesting that available methane will evaporate prior to any significant ethane (Fairall et al., 1996; Mitri et al., 2007). If evaporation is responsible for the depth change, the observed rate of 1.0 ± 0.3 m/year favors a high methane fraction near the surface of the lake. Ethane would impede methane evaporation if the liquid were well mixed. If Ontario were

solely composed of ethane/propane, the observed evaporation rate would require non-physical advection rates to move enough dry air over the lake surface to remove equivalent amounts of liquid.

3.2. North polar region

Titan's hydrocarbon lakes were first identified by Stofan et al. (2007) using SAR data from the north polar region (55–90°N) acquired on July 22, 2006 (T16). Since T16, the north polar region has been imaged by 7 additional SAR passes (Fig. 11) dating between September 2006 (T18) and December 2009 (T64). All but one of these observations were obtained over the course of a nine month period between July 2006 and May 2007, presenting only a short baseline for change detection relative to Titan's 29.5 year seasonal cycle (Table 5). The latest observation of the north polar region (T64), acquired in December 2009, provides up to a 3.5 year baseline between overlapping passes. While there are differences in the appearance of lacustrine features imaged in both T64 and previous passes, initial analysis suggests that, to within observational errors, they can all be explained by variations in viewing geometry. Additional observations of the north polar region, which specifically target areas of expected change, are planned during Cassini's Solstice Mission in May 2012 (T83), September 2012 (T86), May 2013 (T91), July 2013 (T92), October 2013 (T95), August 2014 (T104), and February 2015 (T109).

Table 5
North polar SAR swaths between July 2006 and December 2009. H denotes HiSAR (low resolution SAR acquired outside 25 min from closest approach).

Swath	Acquisition date	L_s (°)	Overlapping observations
T16	July 22, 2006	321	T19, T25, T28
T18	September 23, 2006	323	T25, T28
T19	October 9, 2006	324	T16, T25, T28, T25H, T28H
T25	February 22, 2007	328	T16, T19, T28, T64
T28	April 10, 2007	330	T16, T19, T25, T64
T29	April 26, 2007	331	T16, T18, T19, T25, T28, T64
T30[a]	May 12, 2007	331	T16, T18, T19, T25, T28, T64
T64	Dec. 28, 2009	5	T25, T28

[a] All observations overlapping T30 are with altimetry data, repeat SAR coverage is currently not available for this pass.

The T64 SAR pass was acquired at an average incidence angle of 38° (95% of the distribution of incidence angles is between 24° and 51°). For the primary areas of overlap with T25 and T28 (Fig. 11), this corresponds to an average 19° (8–29°) and 14° (4–23°) higher incidence angle, respectively. As backscatter steeply decreases with increasing incidence in this range, detecting increases in liquid depth on top of backscatter reductions from geometrical variations between T25/T28 and T64 is difficult. As a consequence, backscatter from both empty and partially filled lakes which exist in the overlap area exhibit incidence angle behavior consistent

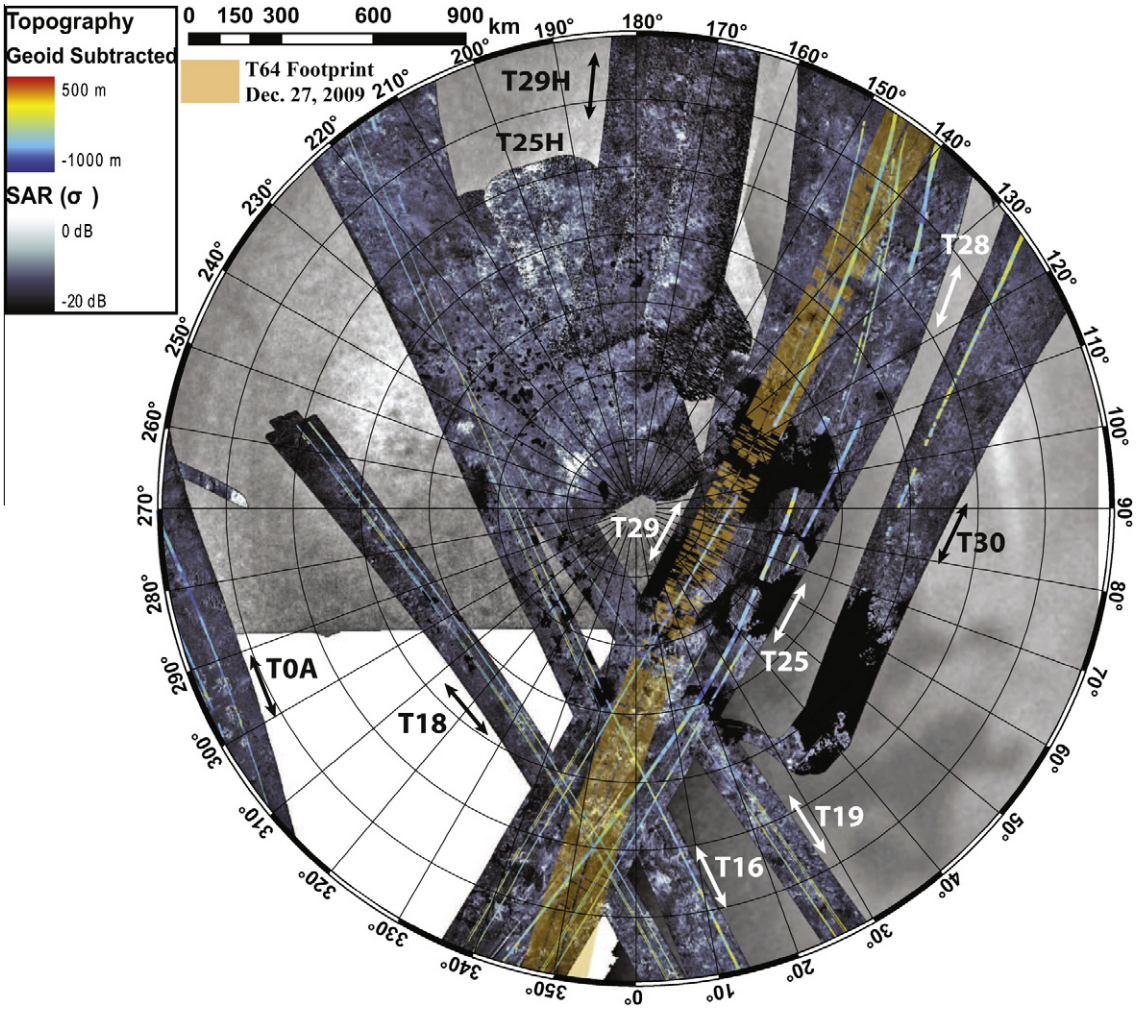

Fig. 11. SAR mosaic of Titan's north polar region (55–90°S) for July 2006 through December 2009 (T16–T64). SAR data has been noise subtracted and corrected for bulk incidence angle effects. Beam positions for T64 repeat coverage is highlighted in orange. ISS images N1551056813 (T25, February 2007), N1592025696 (Rev 72, June 2008), and N1597541984 (Rev81, August 2008) are used as a background.

with the models and lake classifications presented in Section 2 (Fig. 12). To further complicate matters, heavy weather at the Deep Space Network station in Madrid, Spain, during downlink from the spacecraft resulted in partial data loss of T64. While these observations do not unambiguously identify change in lake depth in the north, they do strengthen our confidence in the detectability of change by confirming the incidence angle variation seen in the partially filled and empty classes discussed in Section 2. In addition, the morphologic boundaries of lake and mare shorelines remain unchanged between T64 and earlier observations (Fig. 13). Repeat coverage of the north obtained using the ISS instrument also shows no unambiguous changes in lake distribution as of late 2009 (Turtle et al., submitted for publication).

While the majority of overlapping coverage prior to T64 shows no obvious examples of surface change, there are two features that stand out as having significant backscatter and morphologic differences between passes that may represent temporal variations. In both cases, however, incidence angle variations and opposite side look directions complicate analysis. The first case is a small lake located in the overlap area between T16 and T19. This lake shows an increase of 6–7 dB between incidence angles of 31° (T16) and 16° (T19), but it remains to be seen if this ratio significantly differs from that expected due to geometric effects which are similar in magnitude (3.4–5.4 dB). Mitchell et al. (in preparation) examine this feature in more detail. Additional partially filled lake features in the T16/T19 overlap area also show backscatter ratios ranging between 3 dB and 7 dB. Separating out potentially subtle variations due to surface change from incident and azimuth angle variations

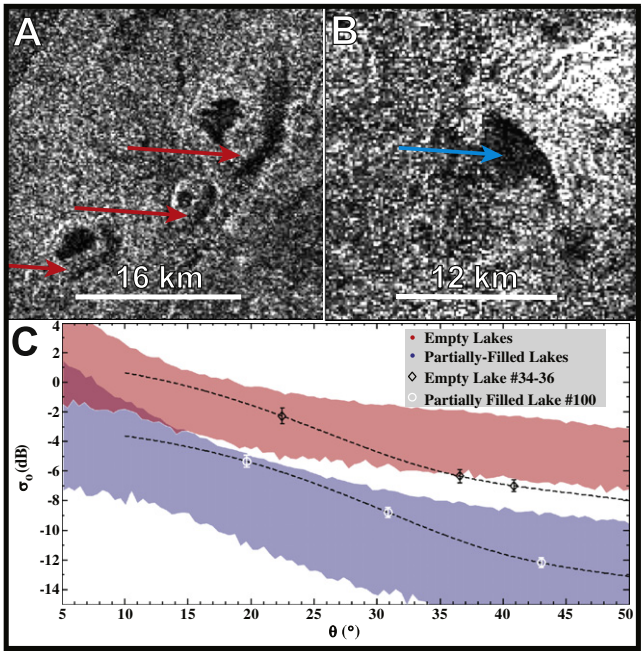

Fig. 12. σ_o for values for empty and partially filled lakes observed during T16, T25, and T28 over a 3.5 year baseline in the north polar region. Images are equicylindrical projections with a logarithmic stretch from −20 dB to 0 dB. (A) Empty lake features (#34–36) with dark lakes partially filling the basin floor. Red arrows indicate areas of empty lake features used in backscatter calculations. The morphologic borders of the dark lakes were invariant across all three observations. (B) Partially filled lake (#100) with blue arrow indicating area used in backscatter calculations. (C) σ_o values for empty lakes #34–36 and partially filled lake #100 plotted on top of empty and partially filled lake classes (see Fig. 1). Dashed lines represent the best-fit Gaussian plus diffuse scattering models for each feature. Model coefficients are listed in Table 1. Note that both features lie within their respective feature classes, unlike the ephemeral features observed in the south polar region.

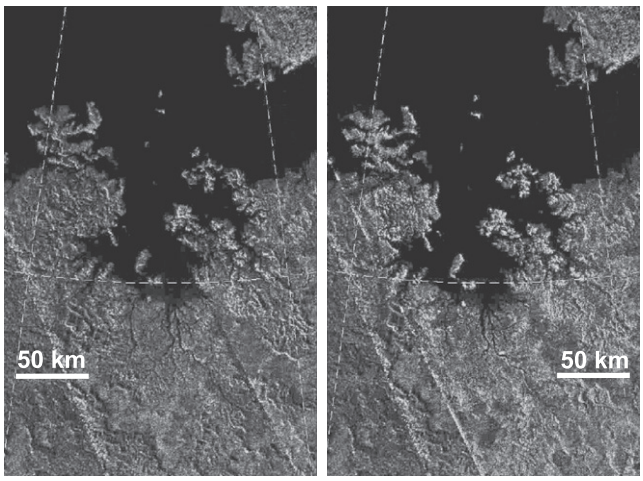

Fig. 13. Stereographic polar projection of the southeast shoreline of Ligea Mare acquired in February 2007 (T25, left) and December 2009 (T64, right). North is up. Note that there is no visible change in shoreline position or channel morphology. Images are corrected for bulk incidence angle variations and presented in a logarithmic stretch from −20 dB to 0 dB.

for these partially filled lakes will require more complex backscatter models than those presented in Section 2 and is the subject of future work.

The second area of significant variation is located in the northern shores of Kraken Mare (Fig. 14). Between February (T25) and April (T28) 2007 this estuary-like morphologic feature, henceforth referred to as Kraken North, exhibits an average backscatter ratio of $\frac{\sigma_{o,\ T25}}{\sigma_{o,\ T28}} \sim 11$ dB (Fig. 14; solid red arrow), with nearby sections of the same feature showing ~2 dB of change (Fig. 14; dashed blue arrows). The incidence angles in this region are 12° ± 2° for T25 and 16° ± 4° for T28. Using the best-fit models presented in Section 2, these angles suggest an expected backscatter ratio of 1.26 ± 0.40 for the background and 1.33 ± 0.45 for the shallow areas of Kraken North. While the average ratio of the surrounding region $\left(\frac{\sigma_{o,\ T25}}{\sigma_{o,\ T28}} = 1.56\right)$ and areas of 2 dB change in Kraken North agree with these predictions, the backscatter ratio of ~11 dB in the central region of Kraken North does not. If incident angle effects can be ruled out, additional explanations for the observed backscatter that can be considered include SAR processing artifacts, look azimuth effects, a deepening of the liquid level, wetting of marshy areas, transient surface roughening by wind or rain, and/or a surface layer with distinct dielectric properties.

The natural shape of the anomalous area argues against radar beam registration errors, boundary effects, or other potential processing artifacts (Fig. 14). Look direction variations are hard to rule out completely, but the homogenous appearance of the various subregions within Kraken North argue against their importance. A meter-scale deepening of a uniform liquid layer could produce an average backscatter reduction of ~11 dB, although there is only weak correlation among σ_o values across the feature (Fig. 14). If the liquid level had changed, σ_o should have been reduced by a fixed ratio. Wetting of initially dry areas in a swamp-like environment can also produce significant reductions in backscatter. However, the anomalous region of Kraken North is still darker than the surrounding terrain and located in the middle of the feature with even darker pixels surrounding it on all sides. Coupling this with the morphology of the drainage network suggests it is unlikely that the anomalous region is dry and topographically above its immediate surroundings. Wind roughening, while appealing because it can influence different sections of a complex shoreline morphology in different ways, would require wind patterns to be restricted to

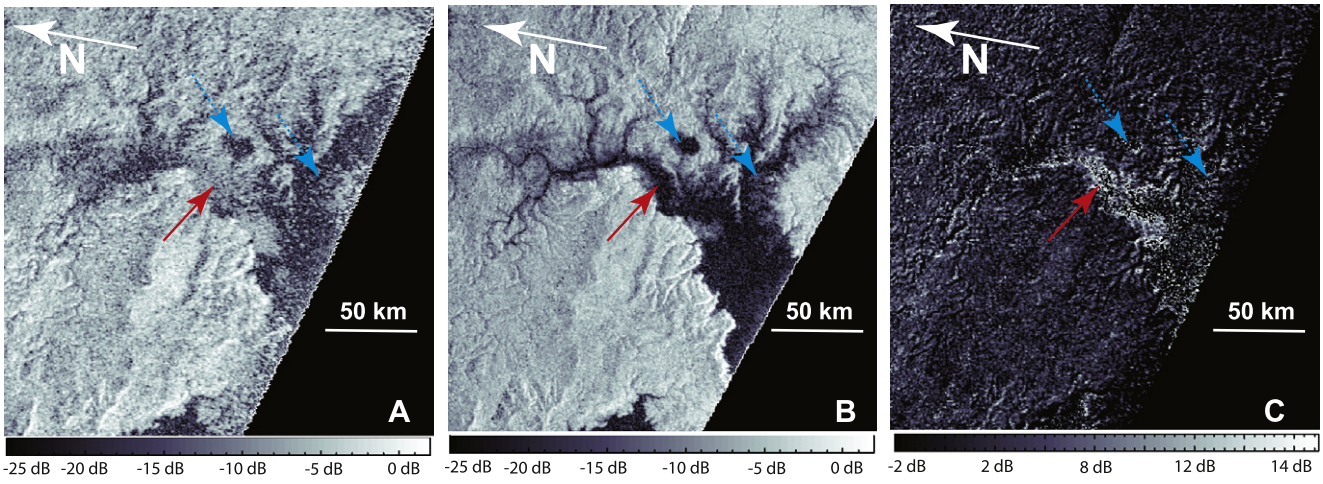

Fig. 14. Stereographic polar projection of Kraken North, an estuary morphology in the northeastern shore of Kraken Mare. (A) Logarithmic stretch of T25 (February 21, 2007). (B) Logarithmic stretch of T28 (April 10, 2007). (C) σ_o ratio of T25/T28 expressed in dB. Images were projected at a resolution of 128 pixels per degree and convolved with a two-pixel diameter box to reduce speckle noise. Areas outside the estuary feature have an average σ_o ratio of 1.57 dB while valid pixels within the estuary have average σ_o ratios of ~11 dB (solid red arrow) and ~2 dB (dashed cyan arrow), with individual pixels of up to 18 dB. However, large portions of Kraken North are below the noise floor in the T28 observation, making interpretation difficult.

the anomalous region of Kraken North. In addition, empirical studies on Earth show that radar backscatter acquired near ~10° incidence is relatively insensitive to wind roughening (Hasselmann et al., 1978). Hasselmann et al. (1978) find that wind roughening decreases σ_o for $\theta < \sim 10°$ and increases it for $\theta > \sim 10°$. Furthermore, an increase of ~11 dB would require RMS wave heights of cm-scale or larger, which have yet to be confirmed on Titan (Wye et al., 2009; Barnes et al., submitted for publication).

The remaining candidate for explaining the backscatter ratio of Kraken North is a transient surface layer with distinct dielectric properties, such as a layer of suspended or floating organic debris present in T25, but not in T28. The suspended or floating (frothy) organic debris causing the higher the σ_o in T25 would then have to sink or disperse by T28, roughly six weeks later. The observed differences are difficult to interpret because of the lower resolution of T25 and the fact that much of Kraken North is below the radar noise floor in T28. Future observations of Kraken Mare and detailed modeling of the effects of organic debris will help to further constrain this hypothesis.

4. Discussion

If the null hypothesis (change in observational geometry) and wave activity are rejected as explanations for ephemeral lake features in Titan's south polar region, remaining possibilities that can explain observed surface changes include evaporation, infiltration, freezing, and cryovolcanism. No evidence for cryovolcanic features has been identified near the study regions (Stofan et al., 2008), so we dismiss this possibility here.

Freezing may occur for a pure methane lake if the temperature of the liquid falls below 91 K (Tokano, 2009a), but this temperature is unlikely near Titan's summer pole. Cassini's Composite Infrared Spectrometry (CIRS) has not observed temperatures below 91 K in the southern high latitudes during summer (Jennings et al., 2009). A recent GCM of Titan predicts physical temperatures remain above 91 K for the latitudes and times of the studied observations (Richardson et al., 2007). While evaporative cooling could further reduce the temperature of the lake, it is highly unlikely that a pure methane lake would be stable long enough to completely freeze (Cordier et al., 2009). Nitrogen would dissolve into the lake from the atmosphere, reducing the freezing temperature by up to 6 K (Lunine, 1993), below the minimum expected temperature reached through evaporative cooling (Mitri et al., 2007). The freezing point is also reduced below the minimum expected temperature if there is a significant fraction of ethane present in the lake (Lunine, 1993).

We prefer liquid evaporation and infiltration as explanations for observed surface change. This hypothesis is supported by the recent discovery of ground fog in the vicinity of Ontario Lacus, a phenomenon which Brown et al. (2009) argues can only exist in the presence of volatile evaporation. Mitri et al. (2007) suggest methane evaporation rates of 0.3–10 m/year can be achieved through advective transport of subsaturated air over a lake surface, assuming horizontal wind speeds of 0.1–1 m/s. Mitchell (2008) estimates that the maximum evaporative flux during southern summer is ~2 W/m^2, corresponding to a methane evaporation rate of ~0.3 m/year. Newman and Richardson (personal communication, 2009) find a maximum evaporation rate of ~1.6 m/year and an average evaporation rate of ~0.5 m/year for the time periods ($340° < L_s < 360°$) and latitudes (60–70°S) in question. Graves et al. (in preparation) find maximum evaporation rates of ~1 m/year and average rates of ~0.5 m/year in the south polar region between southern summer solstice and summer autumnal equinox. Graves et al. (in preparation) further predicts that any liquid remaining in the south polar region during southern winter is predominantly ethane, as the southern methane reservoir is exclusively seasonal in their model. These GCM results, however, represent zonally averaged evaporation. Given that only 0.4% of the observed south polar region is covered in liquid, atmospheric transport could focus available energy over the lakes by warming air parcels and increasing local evaporation. In three-dimensional GCMs, local areas within a latitude bin can typically have evaporation rates a few times higher than the zonal average (Graves and Schneider, personal communication, 2009).

The average 1.0 ± 0.3 m/year loss rate of Ontario Lacus between southern summer solstice and southern autumnal equinox is inconsistent with an ethane-rich composition ($\leqslant$17% CH_4) according to the coupled GCM-sea model presented in Tokano (2009b). A methane-rich composition ($\geqslant$62% CH_4) is consistent with the observed reduction, although Tokano (2009b) estimates a seasonal amplitude of 1–2 m as opposed to the observed 4.0 ± 1.3 m change. The observed ephemeral feature loss rates are also consistent with a predominantly methane composition. In general, the two-layer

model fitting and analysis of receding shorelines at Ontario Lacus result in a liquid loss rate of order 1-m-per-year, roughly consistent with the range of theoretical estimates of methane evaporation.

Available GCMs do not consider flow within a porous medium. However, data returned from the Huygens Probe suggests the presence of a damp porous regolith in Titan's equatorial region, consisting of loosely packed particles ranging in size from silt to medium sand (Lorenz et al., 2006; Zarnecki et al., 2005). Permeability values for these particle sizes, assuming a porosity of 20–30%, can vary by up to six orders of magnitude from 10^{-10} (silt) to 10^{-4} (medium sand) cm^2. Assuming methane as a working fluid, these permeabilities result in hydraulic conductivities (K) varying from 1 to 10^6 m/yr.

Vertical infiltration rates, which describe the rate at which liquid is absorbed into the regolith and are approximated by the hydraulic conductivity, are significantly faster than horizontal seepage rates (Hayes et al., 2008). Complete vertical infiltration would occur on a timescale of $\sim H/K$, where H is the liquid depth. For a 1 m deep lake on Titan, this would correspond to a timescale of 10^{-6}–1 year for the conductivity range above. Hence, the presence of a lake suggests that the regolith is either impermeable or the methane table exists close to the surface. When the methane table is located below the lakebed, we assume that the liquid will vertically infiltrate to the phreatic surface, creating a cylindrical column that will radially flow into the surrounding regolith (Hayes et al., 2008).

The timescale for emptying a lake by radial flow was discussed in Hayes et al. (2008) and can be approximated by $\tau \approx (RD)/(4KH)$, where R is the radius of the liquid and D is the distance it must travel. For a lake depth (H) of 1 m and radius (R) of 5 km, the characteristic time for emptying a lake into the regolith is $\sim$150 years for $K = 10^4$ m/year and $\sim$1.5 years for $K = 10^6$ m/year. For the time difference between T36/T49 (1.2 year) and T39/T55 (1.5 year), horizontal infiltration can only explain the surface change for permeabilities greater than 10^{-4} cm^2, or situations where the methane table is at a distance of order the depth of the lake or greater below the surface. The characteristic separation of features in the ephemeral regions is $\sim$50 km. Horizontal travel over this distance corresponds to timescales of 10^2–10^8 years for the expected permeability range, suggesting these features are not required to co-evolve through subsurface communication, although a common alkanofer table reduction may influence all features by vast vertical infiltration.

In the presence of a porous regolith, infiltration and evaporation are interconnected. While evaporation through a saturated regolith will proceed more slowly than for an exposed lake (Saravanapavan, 2000), the interaction area is significantly greater. Depending on the diffusivity and porosity of the regolith, evaporative loss from the regional alkanofer could be greater than the loss from a lake's surface. If a lake is in interaction with an alkanofer system, its liquid level will drop through vertical infiltration as the volume of material stored in the subsurface reduces. Distinguishing between the importance of interaction with the atmosphere as compared to interaction with a regional subsurface reservoir requires additional observation, particularly the evolution of local clusters of lakes with varying size (Hayes et al., 2008). Observations designed to provide this information have been included in the Cassini Solstice Mission.

5. Summary

Ephemeral surface features have been observed in Titan's south polar region during southern summer. Two regions of overlapping coverage (T39/T55 and T36/T49) contain shallow lakes that transition into features consistent with empty lake basins. On larger scales, the shorelines of Ontario Lacus are observed to recede between ISS and RADAR imagery obtained over a baseline of four years. As of December 2009, no unambiguous changes in liquid level have been observed in the north polar region. While The northern shoreline of Kraken Mare does exhibit backscatter variations that can not be explained by geometric effects alone, the spatial variation of these changes suggest explanations other than varying liquid depth. These observations represent hydrocarbon transport in Titan's dynamic hydrologic system as Saturn approaches northern vernal equinox.

Backscatter cross-sections for empty and partially filled lakes on Titan form consistent and distinct feature classes that can be fit using common backscatter functions. The observed backscatter ratios between T39/T55 and T36/T49, in areas outside the ephemeral features, are consistent with an incidence angle variation produced by these models. The ephemeral features, however, have backscatter variations that are inconsistent with the models and previously observed radar returns without invoking temporal change. Morphologic variations between the observations also imply that ephemeral features in T36/T49 and T39/T55 represent physical surface change.

Liquid reductions of $\sim$1 m/yr are derived from the observations using a simple two-layer model. The shape of the backscatter function for empty and partially filled lake classes supports the use of a simple model to estimate transient liquid depth. Our calculations of liquid loss by evaporation and infiltration are consistent with changes both in the depth of partially filled lakes and complete drying of other lakes.

Analysis of shoreline recession around Ontario Lacus provides an independent measure of loss that is consistent with the modeled ephemeral features. Altimetry profiles intersecting Ontario Lacus provide topographic information used to calculate a loss tangent of $\tan \Delta = (9.2^{+2.5}_{-2.0}) \times 10^{-4}$ for the liquid mixture and generate a near-shore bathymetry map (Hayes et al., in press). Bathymetry slopes inversely correlate to observed shoreline recession magnitudes and suggest 1.0 ± 0.3 m/year loss rates of Ontario Lacus between southern summer solstice and southern autumnal equinox.

Theoretical estimation of methane evaporation rates for the latitudes (60–70°S) and times ($340° < L_s < 360°$) of the ephemeral observations are consistent with the value of $\sim$1 m/year estimated from SAR returns. The reduction in the level of Ontario Lacus agrees with the methane-rich sea model presented in Tokano (2009b). Possible explanations for the observed changes include liquid evaporation and infiltration. Freezing is unlikely given the temperatures and constituents known or suspected to be present in and above the lakes, and there are no cyrovolcanic features identified in the study region. Infiltration into a static hydrologic system is unlikely given the timescales involved. However, infiltration into a dynamic hydrologic system with a regionally varying phreatic surface is possible. These observations demonstrate that Titan's surface plays an active role in its methane cycle and can be used to further constrain volatile transport estimates and describe the evolution of Titan's hydrologic system over both seasonal and orbital time-frames.

Acknowledgments

The authors would like to thank Dr. Jakob Van Zyl of the Jet Propulsion Laboratory for helpful discussions, and the Cassini Engineering Team, without whom the data presented here would not have existed. This work was supported by the Cassini Project, managed by the Jet Propulsion Laboratory, California Institute of Technology, under a contract with the National Aeronautics and Space

Administration, as well as by NASA's Graduate Student Researchers Program.

Appendix A. Supplementary data

Supplementary data associated with this article can be found, in the online version, at doi:10.1016/j.icarus.2010.08.017.

References

Aharonson, O., Hayes, A.G., Lunine, J.I., Lorenz, R.D., Allison, M.D., Elachi, C., 2009. An asymmetric distribution of lakes on Titan as a possible consequence of orbital forcing. Nature Geosci. 2, 851–854. doi:10.1038/ngeo698.

Barnes, J.W., and 14 colleagues, 2009. Shoreline features of Titan's Ontario Lacus from Cassini/VIMS observations. Icarus 201, 217–225. doi:10.1016/j.icarus.2008.12.028.

Barnes, J.W., and 12 colleagues, submitted for publication. Wave constraints for Titan's Jingpo Lacus and Kraken Mare from VIMS Specular Reflection Lightcurves. Icarus.

Barthel, J., Buchner, R., 1991. High frequency permittivity and its use in the investigation of solution properties. Pure Appl. Chem. 63, 1473–1482.

Beckmann, P., Spizzichino, A., 1963. The Scattering of Electromagnetic Waves from Rough Surfaces. Artech House, Inc., Norwood, MA. 511pp..

Black, G.J., Campbell, D.B., Nicholson, P.D., 2001. Icy Galilean satellites: Modeling radar reflectivities as a coherent backscatter effect. Icarus 151, 167–180. doi:10.1006/icar.2001.6616.

Brown, R.H., Soderblom, L.A., Soderblom, J.M., Clark, R.N., Jaumann, R., Barnes, J.W., Sotin, C., Buratti, B., Baines, K.H., Nicholson, P.D., 2008. The identification of liquid ethane in Titan's Ontario Lacus. Nature 454, 607–610. doi:10.1038/nature07100.

Brown, M.E., Smith, A.L., Chen, C., Ádámkovics, M., 2009. Discovery of fog at the south pole of Titan. Astrophys. J. 706, L110–L113. doi:10.1088/0004-637X/706/1/L110.

Brown, R., Lebreton, J.P., Hunter, W., 2010. Titan from Cassini–Huygens. Springer. ISBN:9781402092145.

Campbell, D.B., Black, G.J., Carter, L.M., Ostro, S.J., 2003. Radar evidence for liquid surfaces on Titan. Science 302, 431–434. doi:10.1126/science.1088969.

Cordier, D., Mousis, O., Lunine, J.I., Lavvas, P., Vuitton, V., 2009. An estimate of the chemical composition of Titan's lakes. Astrophys. J. 707, L128–L131. doi:10.1088/0004-637X/707/2/L128.

Daniels, F.B., 1961. A theory of radar reflection from the Moon and planets. J. Geophys. Res. 66, 1781–1788. doi:10.1029/JZ066i006p01781.

Dobson, M.C., Ulaby, F.T., Hallikainen, M.T., El-Rayes, M.A., 1985. Microwave dielectric behavior of wet soil – Part ii: Dielectric mixing models. Geosci. Rem. Sens., IEEE Trans. GE23 (1), 35–46. doi:10.1109/TGRS.1985.289498. ISSN:0196-2892.

Elachi, C., van Zyl, J., 2006. Introduction to the Physics and Techniques of Remote Sensing, second ed. John Wiley. ISBN:100471475696.

Elachi, C., and 34 colleagues, 2005. Cassini RADAR views the surface of Titan. Science 308, 970–974. doi:10.1126/science.1109919.

Fairall, C.W., Bradley, E.F., Rogers, D.P., Edson, J.B., Young, G.S., 1996. Bulk parameterization of air–sea fluxes for tropical ocean-global atmosphere coupled-ocean atmosphere response experiment. J. Geophys. Res. 101, 3747–3764. doi:10.1029/95JC03205.

Grard, R., and 19 colleagues, 2006. Electric properties and related physical characteristics of the atmosphere and surface of Titan. Planet. Space Sci. 54, 1124–1136. doi:10.1016/j.pss.2006.05.036.

Graves, S.D., Schneider, T., Schaller, E.L., Brown, M.E., in preparation. Causes of Titan's lake asymmetry and cloud distribution and prediction of future changes. Nature Geosci.

Hagfors, T., 1964. Backscattering from an undulating surface with applications to radar returns from the Moon. J. Geophys. Res. 69, 3779–3784. doi:10.1029/JZ069i018p03779.

Hagfors, T., 1970. Remote probing of the Moon by infrared and microwave emission and by radar. Radio Sci. 5, 189–227. doi:10.1029/RS005i002p00189.

Hargreaves, J.K., 1959. Radio observations of the lunar surface. In: Proceedings of the Physical Society of London, May 1959, pp. 536–537.

Hasselmann, K., and 20 colleagues, 1978. Radar measurements of wind and waves. Boundary-Layer Meteorol. 13, 405–412. doi:10.1007/BF00913885.

Hayes, A.G., and 13 colleagues, 2008. Hydrocarbon lakes on Titan: Distribution and interaction with a porous regolith. Geophys. Res. Lett. 35, 9204–9208. doi:10.1029/2008GL033409.

Hayes, A.G., Wolf, A.S., Aharonson, O., Zebker, H., Lorenz, R., Paillou, P., Wall, S., Elachi, C., in press. Bathymetry and absorptivity of Titan's Ontario Lacus. J. Geophys. Res., in press. doi:10.1029/2009JE003557.

Iess, L., Rappaport, N.J., Jacobson, R.A., Racioppa, P., Stevenson, D.J., Tortora, P., Armstrong, J.W., Asmar, S.W., 2010. Gravity field, shape, and moment of inertia of Titan. Science 327, 1367–1369. doi:10.1126/science.1182583.

Janssen, M.A., 17 colleagues, and the Cassini RADAR Team, 2009. Titan's surface at 2.2-cm wavelength imaged by the Cassini RADAR radiometer: Calibration and first results. Icarus 200, 222–239. doi:10.1016/j.icarus.2008.10.017.

Jennings, D.E., and 19 colleagues, 2009. Titan's surface brightness temperatures. Astrophys. J. 691, L103–L105. doi:10.1088/0004-637X/691/2/L103.

Kirk, R.L., 16 colleagues, and the Cassini RADAR Team, submitted for publication. High resolution topographic models of Titan's surface derived by radar stereogrammetry with a rigorous sensor model. Icarus 112.

Le Gall, A., Janssen, M.A., Paillou, P., Lorenz, R.D., Wall, S.D., and the Cassini RADAR Team, 2010. Radar-bright channels on Titan. Icarus 207, 948–958. doi:10.1016/j.icarus.2009.12.027.

Lopes, R.M.C., 24 colleagues, and Cassini RADAR Team, 2010. Distribution and interplay of geologic processes on Titan from Cassini RADAR data. Icarus 205, 540–558. doi:10.1016/j.icarus.2009.08.010.

Lorenz, R.D., 1994. Crater lakes on Titan: Rings, horseshoes and bullseyes. Planet. Space Sci. 42, 1–4. doi:10.1016/0032-0633(94)90134-1.

Lorenz, R.D., Niemann, H.B., Harpold, D.N., Way, S.H., Zarnecki, J.C., 2006. Titan's damp ground: Constraints on Titan surface thermal properties from the temperature evolution of the Huygens GCMS inlet. Meteorit. Planet. Sci. 41, 1705–1714.

Lorenz, R.D., Jackson, B., Hayes, A., 2010a. Racetrack and Bonnie Claire: Southwestern US playa lakes as analogs for Ontario Lacus, Titan. Planet. Space Sci. 58, 724–731. doi:10.1016/j.pss.2009.05.012.

Lorenz, R.D., Newman, C., Lunine, J.I., 2010b. Threshold of wave generation on Titan's lakes and seas: Effect of viscosity and implications for Cassini observations. Icarus 207, 932–937. doi:10.1016/j.icarus.2009.12.004.

Lunine, J.I., 1993. Does Titan have an ocean? A review of current understanding of Titan's surface. Rev. Geophys. 31, 133–149. doi:10.1029/92RG02794.

Mitchell, J.L., 2008. The drying of Titan's dunes: Titan's methane hydrology and its impact on atmospheric circulation. J. Geophys. Res. (Planets) 113 (E8015), 1–22. doi:10.1029/2007JE003017.

Mitchell, K.L., 10 colleagues, and the Cassini RADAR Team, in preparation. Titan's north polar lake district: Insights from the Cassini Titan Radar Mapper. Icarus.

Mitri, G., Showman, A.P., Lunine, J.I., Lorenz, R.D., 2007. Hydrocarbon lakes on Titan. Icarus 186, 385–394. doi:10.1016/j.icarus.2006.09.004.

Muhleman, D.O., 1995. Earth-based remote sensing of Solar System objects. Rev. Geophys. 33, 477–480. doi:10.1029/95RG00555.

Newman, C.E., Richardson, M.I., Lee, C., Toigo, A.D., Ewald, S.P., 2008. The TitanWRF model at the end of the Cassini Prime Mission. AGU Fall Meeting, p. A2 (abstracts).

Ostro, S.J., and 11 colleagues, 1992. Europa, Ganymede, and Callisto: New radar results from Arecibo and Goldstone. J. Geophys. Res. 97, 18277–18244.

Ostro, S.J., 18 colleagues, and the Cassini RADAR Team, 2006. Cassini RADAR observations of Enceladus, Tethys, Dione, Rhea, Iapetus, Hyperion, and Phoebe. Icarus 183, 479–490. doi:10.1016/j.icarus.2006.02.019.

Paillou, P., Lunine, J., Ruffié, G., Encrenaz, P., Wall, S., Lorenz, R., Janssen, M., 2008a. Microwave dielectric constant of Titan-relevant materials. Geophys. Res. Lett. 35 (L18202), 1–4. doi:10.1029/2008GL035216.

Paillou, P., Mitchell, K., Wall, S., Ruffié, G., Wood, C., Lorenz, R., Stofan, E., Lunine, J., Lopes, R., Encrenaz, P., 2008b. Microwave dielectric constant of liquid hydrocarbons: Application to the depth estimation of Titan's lakes. Geophys. Res. Lett. 35, L05202, 1–5. doi:10.1029/2007GL032515.

Pierson Jr., W.J., Moskowitz, L., 1964. A proposed spectral form for fully developed wind seas based on the similarity theory of S.A. Kitaigorodskii. J. Geophys. Res. 69, 5181–5190. doi:10.1029/JZ069i024p05181.

Pollack, J.B., Cuzzi, J.N., 1980. Scattering by nonspherical particles of size comparable to wavelength – A new semi-empirical theory and its application to tropospheric aerosols. J. Atmos. Sci. 37, 868–881. doi:10.1175/1520-0469(1980)037.

Press, William, Flannery, Brian, Teukolsky, Saul, Vetterling, William, 1992. Numerical Recipes in C: The Art of Scientific Computing. Cambridge University Press. ISBN:0521431085.

Rice, S.O., 1951. Small perturbation method. Commun. Pure Appl. Math. 4, 251–378.

Richardson, M., Toigo, A., Newman, C., 2007. PlanetWRF: A general purpose, local to global numerical model for planetary atmospheric and climate dynamics. J. Geophys. Res. 112 (E09001), 1–29.

Rignot, E.J., Ostro, S.J., van Zyl, J.J., Jezek, K.C., 1993. Unusual radar echoes from the Greenland Ice sheet. Science 261, 1710–1713.

Saravanapavan, S.O., 2000. Molecular diffusivity. Commun. Pure Appl. Math. 4, 251–378.

Sen, A.D., Anicich, V.G., Arakelian, T., 1992. Dielectric constant of liquid alkanes and hydrocarbon mixtures. J. Appl. Phys. 25, 512–521.

Simpson, R.A., Tyler, G.L., 1982. Radar scattering laws for the lunar surface. IEEE Trans. Antennas Propagation 30, 438–449. doi:10.1109/TAP.1982.1142803.

Stiles, B.W., 18 colleagues, and the Cassini RADAR Team, 2009. Determining Titan surface topography from Cassini SAR data. Icarus 202, 584–598. doi:10.1016/j.icarus.2009.03.032.

Stofan, E.R., and 37 colleagues, 2007. The lakes of Titan. Nature 445, 61–64. doi:10.1038/nature05438.

Stofan, E.R., 14 colleagues, and Cassini RADAR Team, 2008. Varied geologic terrains at Titan's south pole: First results from T39. In: Lunar and Planetary Institute Science Conference, vol. 39, p. 1491 (abstracts).

Sultan-Salem, A.K., Tyler, G.L., 2006. Generalized fractal-based laws for scattering from planetary surfaces: A unifying scale-explicit paradigm. J. Geophys. Res. (Planets) 111 (E06S08), 1–6. doi:10.1029/2005JE002540.

Thompson, W.R., Squyres, S.W., 1990. Titan and other icy satellites – Dielectric properties of constituent materials and implications for radar sounding. Icarus 86, 336–354. doi:10.1016/0019-1035(90)90224-W.

Tokano, T., 2009a. Limnological structure of Titan's hydrocarbon lakes and its astrobiological implication. Astrobiology 9, 147–164. doi:10.1089/ast.2007.0220.

Tokano, T., 2009b. Impact of seas/lakes on polar meteorology of Titan: Simulation by a coupled GCM–Sea model. Icarus 204, 619–636. doi:10.1016/j.icarus.2009.07.032.

Turtle, E.P., Perry, J.E., McEwen, A.S., DelGenio, A.D., Barbara, J., West, R.A., Dawson, D.D., Porco, C.C., 2009. Cassini imaging of Titan's high-latitude lakes, clouds, and south-polar surface changes. Geophys. Res. Lett. 36, L2204. doi:10.1029/2008GL036186.

Turtle, E.P., Perry, J.E., Hayes, A.G., McEwen, A.S. Shoreline retreat at Titan's Ontario Lacus and Arrakis Planitia from Cassini Imaging Science subsystem observations. Icarus. submitted for publication.

Tyler, G.L., Simpson, R.A., Maurer, M.J., Holmann, E., 1992. Scattering properties of the Venusian surface – Preliminary results from Magellan. J. Geophys. Res. 97 (13), 115–139.

Ulaby, F.T., Moore, R.K., Fung, A.K., 1982. In: Ulaby, F.T. (Ed.), Microwave Remote Sensing: Active and Passive, vol. 2. Artech House, Norwood, MA.

Wall, S., and 20 colleagues, 2010. Active shoreline of Ontario Lacus, Titan: A morphological study of the lake and its surroundings. Geophys. Res. Lett. 37, L5202. doi:10.1029/2009GL041821.

West, R.D., and 19 colleagues, 2008. Cassini RADAR sequence planning and instrument performance. IEEE Trans. Geosci. Rem. Sens., pp. 1777–1795. doi:10.1109/TGARS.2008.2007217.

Wye, L.C., Zebker, H.A., Ostro, S.J., West, R.D., Gim, Y., Lorenz, R.D., and the Cassini RADAR Team, 2007. Electrical properties of Titan's surface from Cassini RADAR scatterometer measurements. Icarus 188, 367–385. doi:10.1016/j.icarus.2006.12.008.

Wye, L.C., Zebker, H.A., Lopes, R.M., Peckyno, R., Le Gall, A., Janssen, M.A., 2008. Surface parameters of Titan feature classes from Cassini RADAR backscatter measurements. AGU Fall Meeting, p. A1318 (abstracts).

Wye, L.C., Zebker, H.A., Lorenz, R.D., 2009. Smoothness of Titan's Ontario Lacus: Constraints from Cassini RADAR specular reflection data. Geophys. Res. Lett. 36, L16201. doi:10.1029/2009GL039588.

Zarnecki, J.C., and 25 colleagues, 2005. A soft solid surface on Titan as revealed by the Huygens Surface Science Package. Nature 438, 792–795. doi:10.1038/nature04211.

Zebker, H.A., Stiles, B., Hensley, S., Lorenz, R., Kirk, R.L., Lunine, J., 2009. Size and shape of Saturn's moon Titan. Science 324, 921–923. doi:10.1126/science.1168905.